Laser Ablation (U-Th-Sm)/He Dating of Zircons: Analytical Age Bias and its Consequence for Studying Detrital Zircon Populations

Julien Léger, Raphaël Pik, Bouchaïb Tibari, Sébastien Ternois, Mary Ford, Chantal Peiffert, Julien Mercadier

To cite this version:

Julien Léger, Raphaël Pik, Bouchaïb Tibari, Sébastien Ternois, Mary Ford, et al.. Laser Ablation (U-Th-Sm)/He Dating of Zircons: Analytical Age Bias and its Consequence for Studying Detrital Zircon Populations. Geostandards and Geoanalytical Research, 2023, 47 (2), pp.219-242. ⟨10.1111/ggr.12494⟩. ⟨insu-04360176⟩

HAL Id: insu-04360176

https://insu.hal.science/insu-04360176v1

Submitted on 8 Sep 2025

Laser Ablation (U-Th-Sm)/He Dating of Zircons: Analytical Age Bias and its Consequence for Studying Detrital Zircon Populations

Julien **Léger** (1)*, Raphaël **Pik** (1), Bouchaïb **Tibari** (1), Sébastien **Ternois** (2), Mary **Ford** (1), Chantal **Peiffert** (3) and Julien **Mercadier** (3)

(1) Université de Lorraine, CNRS, CRPG, UMR7358, F-5400, Nancy, France
(2) Université d’Orléans, CNRS, ISTO, UMR 7327, F-45071 Orléans, France
(3) Université de Lorraine, CNRS, GeoRessources, F-54000, Nancy, France
*Corresponding author. e-mail: julien.leger@univ-lorraine.fr

Abstract

The *in situ* (U-Th-Sm)/He and U/Pb laser-ablation double-dating procedure is a valuable method that can provide a large dataset relatively efficiently in contrast with conventional bulk helium thermochronometry. In this study, we evaluate the potential age error associated with the double ablation procedure and report the *in situ* (U-Th-Sm)/He double-ablation dating of 249 zircons from the Fish Canyon Tuff locality. With LA-ICP-MS pseudo-depth profiling and 3D numerical modelling, we show that the concentric double-ablation procedure in minerals with U-Th-Sm zoning can generate a significant (U-Th-Sm)/He age error (positive or negative), resulting in over-scattering and/or an offset of the mean age. Pseudo-depth profiling is insufficient to predict the individual age error, partly because of the superimposed ablations. To evaluate the consequence of this inherent bias, we confront a synthetic age distribution to the error expected for U-Th-Sm zoned zircons analysed with double-ablation (U-Th-Sm)/He thermochronometry. As expected, a strong age bias causes the spreading of peak ages, downgrading the original signal. Yet, the throughput of the ablation-based method can allow intra- and inter-sample peak age identification and comparison, and the coupling of (U-Th-Sm)/He and U/Pb ages extends our ability to deconvolute a multimodal age spectrum.

Keywords: thermochronology, zircon, detrital, double-ablation, double-dating, Fish Canyon Tuff, LA-ICP-MS, depth-profiling.

Received 08 Aug 22 – Accepted 06 Mar 23

Detrital geochronology is a commonly used method for studying orogenic processes and their interactions, such as tectonic and landscape evolution in foreland basins and their source terrains (e.g., Vacherat *et al*. 2017, Jourdan *et al*. 2018). In particular, the use of low temperature thermochronometry (e.g., fission tracks and the (U-Th-Sm)/He system) on detrital zircons (DZ) allows quantification of long-term denudation dynamics (e.g., Whitchurch *et al*.

2011). Zircon is also a suitable mineral for U/Pb dating and source-to-sink studies based on the analysis of detrital age spectra.

Historically, (U-Th-Sm)/He and U/Pb dating were first performed on different zircon batches, which prevented the coupling of these ages, and may have led to erroneous peak-to-peak matching between age distributions. Pioneer works of Rahl *et al*. (2003), Campbell *et al*. (2005), Filleaudeau *et al*. (2011), and Tripathy-Lang *et al*. (2013) provided the first coupled (U-Th-Sm)/He and U/Pb single-grain zircon dating, involving firstly an *in situ* U/Pb analysis (SIMS, LA-ICP-MS), and secondly a bulk measurement and crystal dissolution for the (U-Th-Sm)/He dating (i.e., conventional helium thermochronometry, see Tibari *et al*. 2016). A strong bias of conventional (U-Th-Sm)/He thermochronology is related to U-Th-Sm zoning, as demonstrated by Dobson *et al*. (2008). The age bias emerges when the true quantity of ^{4}He loss is different compared with the one predicted by the classical alpha-ejection correction factor, the latter being calculated solely according to crystal geometry, thus not taking into account the U-Th-Sm heterogeneity at the grain scale. Hourrigan *et al*. (2005) demonstrated that age errors can reach up to ~ 30% when the U-Th-Sm zircon heterogeneity is not properly accounted for. Even with this being known, documenting the U-Th-Sm heterogeneity for all the detrital grains would involve significantly longer chemical characterisation. In summary, conventional thermochronometry relies on well-established analytical procedures, but the experimental time needed (especially crystal dissolution, U-Th-Sm quantification at the grain scale, and grain unmounting) makes it a low production method, conflicting with the dating throughput needed by a provenance study (see Vermeesch 2012).

A major advance was made with the development of the coupled *in situ* (U-Th-Sm)/He and U/Pb double-dating procedure (also referred to as non-conventional thermochronometry) applied to detrital zircons (Tripathy *et al*. 2010, Evans *et al*. 2015, Horne *et al*. 2016). This procedure relies on two separate phases of laser ablation analyses. One first ablation is performed to determine the radiogenic helium content, and a second to determine the U-Th-Sm-Pb isotopic amount ratios and mass fractions with the use of LA-ICP-MS. The emplacement and geometry of ablations have differed between authors. Horne *et al*. (2016) performed concentric ablations, with equal radius and depth. The U-Th-Sm sampling site exceeds the dimension of the helium pit of around 20 µm, in order to mobilise the likely radioactive contributors of the measured ^{4}He. Meanwhile, Evans *et al*. (2015) performed a shallow but wide first ablation for helium prior to a deeper but narrower ablation for U-Th-Sm. In both cases, the non-conventional ablation-based dating strategy makes it possible to double-date > 100 zircons for a given sample, compared with ~ n = 10–30 zircons using the conventional bulk method with roughly the same analytical effort.

The *in situ* technique has differences compared with the bulk method: first, the laser-ablation technique provides a significantly lower quantity of helium compared with bulk degassing, due to the relatively lower volume of material ablated, and therefore comes with higher uncertainties with respect to the ^{4}He content; second, U-Th-Sm zoning and alpha-redistribution, on the same basis as conventional thermochronometry, may lead to a bias in the measured age, as the measured ^{4}He content may not be representative of the measured radioactive U-Th-Sm. This latter phenomenon has been discussed to some extent (Vermeesch *et al*. 2012, Horne *et al*. 2016, Pickering *et al*. 2020) but no attempt has been made to quantitatively account for it; third, it is unclear if the benefit of dating more grains via the *in situ* procedure can compensate the disadvantage of a poorer dating precision, when DZ are studied in a source-to-sink approach.

In order to investigate these features, this study first provides a new dataset of 249 *in situ* (U-Th-Sm)/He double-ablation ages of zircon reference material from the Fish Canyon Tuff (zFCT) locality. These are combined with a methodology for LA-ICP-MS data treatment to quantify U-Th-Sm zoning. The method is based on an estimation and correction of the laser-ablation down-hole fractionation, which allows us to determine, with the use of a simple estimator, the eU variation (eU for effective uranium, eU = U + 0.235*Th) along the pseudo-depth profile in the grain. A 3D numerical forward modelling is presented to understand and evaluate how the *in situ* double-ablation micro-sampling strategy can affect the calculated thermochronometric age. Finally, we use zFCT data to compare the relevance of the double-ablation and conventional dating procedures when they are used in a long-term detrital zircon thermochronology study of a foreland basin, considering the U-Th-Sm-zoning related bias and the number of grains that are commonly dated.

Materials and methods

Analytical protocol for (U-Th-Sm)/He thermochronometry

Fish Canyon Tuff (FCT):

- Characterisation from previous studies. The Fish Canyon Tuff (FCT) is an ignimbrite sheet of dacitic composition, emitted from the La Garita caldera in the San Juan volcanic field of Colorado (e.g., Lipman *et al*. 1970, Lipman *et al*. 1997, Bachmann *et al*. 2007). The FCT provides minerals, either phenocrysts or accessories, that serve as reference materials for high- and low-temperature thermochronometry, for example: zircons for U/Pb, (U-Th-Sm)/He (i.e., ZHe), and fission-track (i.e., ZFT) dating; titanites for U/Pb and (U-Th-Sm)/He dating; apatites for (U-Th-Sm)/He (i.e., AHe), and fission-track (i.e., AFT) dating; sanidine, biotite, and hornblende for K-Ar and Ar-Ar dating. In the following, zircons from the FCT locality will be referred to as zFCT.

Two sampling sites are classically described for the Fish Canyon Tuff, as summarised by Gleadow *et al*. (2015): (1) the “proximal” site (relative to the caldera) is located near the South Fork locality, where the ignimbrite sheet is relatively thick (> 400 m thickness). It is the “classic” sampling site, located at the base of the FCT, however, Gleadow *et al*. (2015) extended the sampling to the whole vertical section of the FCT; (2) the second site is referred to as “distal” is located along the Del Norte meridian where the ignimbrite sheet is much thinner (< 100 m).

Zircons from the FCT have been thoroughly described in numerous radiochronometric studies. For the “classic” sampling site, a U/Pb Concordia age (sense of Ludwig *et al*. 1998) of 28.476 ± 0.029 Ma (2*s*) was obtained with ID-TIMS by Schmitz and Bowring (2001). Based on their distribution of disequilibrium-corrected ^{206}Pb/^{238}U ages Bachmann *et al* (2007) refined the magmatic history of the FCT and argued for a magma residence time of > 0.3 My.

Gleadow *et al*. (2015) compared the zircon (ZHe) and apatite (AHe) (U-Th-Sm)/He conventional ages at the proximal and distal sampling sites. For apatites, the "classic" site exhibits low AHe ages of 20.8 ± 0.8 Ma (inverse-variance weighted mean, ivwm, 2*s*), in contrast to the rest of the sampling (comparatively shallower) that provides AHe comprised between 27.6 ± 2.0 Ma and 29.5 Ma ± 0.8 (ivwm, 2*s*). The authors explain this ~ 8 My difference by a post-eruption cooling due to the deep stratigraphic position of the "classic" site. For zircons, no significant difference was revealed between ZHe ages of distal and proximal sites, thus including the "classic" site. Looking more closely at individual ages, it however appears the "classic" site provided a narrower distribution of ZHe ages compared with the rest of their sampling, either proximal or distal.

Horne *et al*. (2016) provide *in situ* laser-ablation (U-Th-Sm)/He and U/Pb double-dating on zircons and titanites from the FCT. They report an age for ZHe of 28.38 ± 0.73 Ma (ivwm, 2*s* multiplied by $\text{MSWD}^{1/2}$) with a MSWD value of 4.58. By comparison, their conventional dating provides less widely scattered results but a similar mean age, with an age for ZHe of 28.16 ± 0.24 Ma (ivwm, 2*s* multiplied by $\text{MSWD}^{1/2}$) with a reported MSWD of 12.62.

- Sample preparation. Rocks from the FCT locality were sampled in the "classic" site (see Naeser *et al*. 1981), located ~ 9 km SW of South Fork, Colorado, along the U.S. Highway 160. Samples were crushed using a jaw crusher and then a double roller mill, before the sieving operation that retrieved > 250 µm, > 125, and > 75 µm granulometric fractions. Dense minerals among the 250–125 µm and 125–75 µm fractions were pre-concentrated with a vibrating table, before going through a Frank magnetic separator to remove the magnetic minerals. Finally, the minerals with a density above or near 3.3 g cm^{-3} were collected using heavy-liquid separation and constituted our zFCT stock. This zFCT stock was hand-picked over more than two years and by several operators. The mounting operation involves the deposition of grains on a glass slide, heating around 310 °C and pressure-assisted incorporation of grains in a molten PTFE (Teflon®) sheet. Abrasion and polishing are performed by hand with silicon carbide (SiC) sandpaper and diamond paste (6 µm, 3 µm, 1 µm). A short ultrasonic washing is finally performed on the medium to clean it.

Here we report the dating of three batches of FCT, analysed between 2019 and 2021, which were used as QC for the *in situ* double-ablation analyses performed at the CRPG laboratory. The first batch FCT-A comprises zircons with minimal (100)-face widths ranging mostly between 90 and 110 µm and handpicked when the zFCT stock was complete. The FCT-B and FCT-C batches were handpicked consecutively, from the depleted zFCT stock, and therefore provided zircons with a minimal (100)-face width ranging mostly between 75 µm and 95 µm.

Hand-picked grains were checked for inclusions under a binocular microscope, and ablations were performed in order to avoid those. For batch FCT-A, cathodoluminescence (CL) images were acquired using a TESCAN VEGA3 LM conventional scanning electron microscope (SEM) equipped with a Gatan ChromaCL2UV CL detector at SCMEM (Service Commun de Microscopie Électronique et de

Microanalyse X, GéoRessources, Université de Lorraine, France), operated under partial pressure. No metallisation was performed on the surface of the samples.

^{4}He determination: Radiogenic helium measurements were conducted in the CRPG noble-gas facility (Université de Lorraine, Nancy, France). *In situ* micro-sampling was performed under ultra-high vacuum (UHV) using an ESI NWR193 Excimer ArF laser-system with a 193 nm wavelength. The laser was operated with fluence around 2–3 J cm^{-2}, calibrated with an independent calibration device by the manufacturer Coherent. Ablations were performed with a cylindrical shape with both radius and depth of 15 µm (Figure 1). The number of laser pulses varied between 300 and 375 depending on the fluence, with a repetition rate of 5 Hz.

The ablated materials were purified using a UHV line composed of getters and a cryogenic cold head. Isotope dilution was performed with a ^{3}He spike. Finally, mass analysis was conducted using a MKS Microvision 2 Residual Gas Analyser, with a correction on the intensity of mass 3 peak due to the isobaric interference of H_2H (HD) and H_3^+ and checking for isotopic fractionation by measuring the mass 3 / mass 4 of a reference gas.

The topography of ablated crystals was obtained using a Zygo ZeGage Pro HR, interferometry-based, optical profilometer with a 50X magnification lens with a vertical resolution around 0.15 nm. The raw acquisition was converted to topography with the Mx^{TM} software provided by Zygo manufacturer, with the following steps: (1) suppression of spiky numerical artefacts; (2) correction of the sample tilt; (3) interpolation of void values, typically located along the steep walls of ablation pits; (4) definition of the reference plane with three mask selections around the ablated area; (5) definition of the ablation region with a mask selection; (6) estimation of the ablated volume.

The ablation performed with the NWR193 often left loose residuals at the bottom of the pit. This material was removed before measuring the ablation volume, otherwise it resulted in an underestimated volume and thus overestimated ^{4}He content. The samples were thus gently cleaned using a short ultrasonic bathing, being careful not to unmount the ablated crystals.

< Figure 1 here >

U-Th-Sm data acquisition and treatment:

- Data acquisition. U-Th-Sm analyses were performed at the GeoRessources laboratory (Université de Lorraine, Nancy, France), with a LA-ICP-MS composed of an ESI NWR193 excimer laser system with a 193 nm wavelength coupled to an Agilent 8900 quadrupole mass spectrometer. Laser fluence was set to 5 J cm^{-2} with spot diameter of 60 µm and a repetition rate of 5 Hz. Laser ablation occurred over 300 pulses (~ 60 s) to reach around 30 µm depth (see Figure 1). Because the U-Th-Sm ablation is superimposed onto the first, smaller, helium ablation, the final depth profile is not purely cylindrical (see Pickering *et al*. 2020 for instance).

Helium was used as the carrier gas for ablation (600 to 750 ml min^{-1}) and mixed with argon gas (650 to 750 ml min^{-1}, depending on the daily instrument tuning). The ablation chamber was an ESL two-cell ‘TwoVol2’, which strongly enhances the transport of ablated materials, reduces the wash-out delay and therefore minimises the averaging effect for an analyte along the vertical ablation. The background signal was recorded over 30 s before each ablation and wash-out was conducted over ~ 10 s.

Silicon measured with the mass 29 (^{29}Si) was chosen as the internal standard element and its value in unknown zircons is derived from its stoichiometric proportion (around 14.75% *m/m*, or 10^2 g g^{-1} Zr). The complete list of measured masses and their respective dwell times are described in online supporting information Tables S1–S3. Standard bracketing was conducted to evaluate the temporal drift of the instrument and to account for inter-element mass discrimination.

A typical acquisition batch consisted of ten to fifteen unknown analyses bracketed by two rounds of reference material analyses. NIST synthetic glasses (NIST SRM 610 and NIST SRM 612, Jochum *et al*. 2011) were used as reference materials for U-Th-Sm and other REE mass fractions determination, and 91500 (Wiedenbeck *et al*. 1995, 2004) and Plešovice (Sláma *et al*. 2008) natural zircons were used as reference materials for the determination of the various U-Pb isotopic amount ratios.

- Data treatment. Each of the time-series was inspected to reject damaged or undersized zircons, based on their silicon ICP-MS signals. The analyte mass fraction determination procedure was derived from that proposed by Longerich *et al*. (1996), but also corrected for the down-hole fractionation (DF) effect. An in-house Matlab® program was used, checked on with the Iolite software (Paton *et al*. 2010). The estimation of the DF effect was based on the analysis of a homogeneous material (NIST SRM 610 and SRM 612 synthetic glass).

Correcting the DF effect did not change the final mean value of the analyte mass fraction, but it allows for identification of any intensity variation of the time-resolved signals with respect to the ablation depth. For LA-ICP-MS signals, the DF effect was defined by a linear model, which allowed a straightforward correction (see Figure 2).

From the pseudo-depth variation of the analyte mass fraction was finally extract the normalised linear slope, which roughly reflects the amplitude of variation of the analyte mass fraction between the top and bottom of the ablation. This approach was conducted on eU signals of all dated crystals, with the following steps: (1) calculation of a linear fit applied to the eU pseudo-depth series, which were previously corrected for down-hole fractionation (2) then, the slope of the linear fit was divided by the median value of the fit to obtain the normalised eU slope (µg g^{-1} / µm / µg g^{-1}, or µm^{-1}) (Figure 2).

< Figure 2 here >

Forward numerical modelling of the (U-Th-Sm)/He system and double-ablation strategy

Forward numerical modelling was conducted on an idealised spherical crystal and consists of two separate steps. Firstly, the diffusion, α-redistribution, and α-ejection processes for the (U-Th)/He system in zircon (^{147}Sm was not considered) are modelled using both the partial differential equation solver toolbox of MATLAB® software and personal algorithms. The redistribution and loss processes were dealt with together with a probabilistic approach, where the local retentivity is calculated from the possible α-contributors neighbours. The mean travelling distance values for ^{238}U, ^{235}U and ^{232}Th of Ketcham *et al*. (2011) are used. The diffusion model is based on the work of Guenthner *et al*. (2013), with damage and annealing dependency. The time-temperature path is invariant, the crystal being held at 20 °C for 28.4 Ma.

Secondly, the double-ablation micro-sampling strategy was reproduced, with ablation pits performed consecutively and concentrically, following our measurement procedure (Figure 1), inspired from Horne *et al*. (2016). The following features were considered: the modelled crystal is abraded to its equatorial plane, ablations are performed at the centre of the grain, and ablated materials of the helium ablation pit cannot be remobilised for U-Th-Sm measurement (see Figure 3). However, the numerical modelling did not reproduce the complex depth-profile obtained on actual measurements (e.g., Pickering *et al*. 2020), because it would have required a modelling effort outside the scope of this first-order approach. Instead, it was assumed a final cylindrical depth-profile after the U-Th-Sm ablation.

< Figure 3 here >

Finally, the LA-ICP-MS depth-series for eU mass fraction was modelled, and the procedure described in the previous section was used to determine the normalised eU slope value. Two different zoning patterns were studied in our models: a linear variation from grain core to grain rim, and a step variation with a varying radial position. Oscillatory zoning was not specifically studied here, only monotonous radial zoning. Our aim is not to accurately describe specific zoning patterns, but instead to investigate the extent to which the zoning and the double-ablation strategy can bias the measured age. In the model input, U and Th distribution can vary according to the geometrical zoning, with mass fractions restricted to the mean range of natural zFCT data acquired (100 to 1000 µg g^{-1}) (see Figure 4). The conventional age was also extracted from the numerical outputs. No correction regarding the alpha-redistribution was performed, and conventional ages were only corrected with an alpha-ejection factor. For both dating procedures, the age error, i.e., the difference between the reference age and the measured age, directly reflects the amount of bias induced by eU zoning and the measurement strategies.

< Figure 4 here >

Results

In situ double-ablation (U-Th-Sm)/He dating of FCT zircons

The formulae used for statistical estimators are presented in Appendix A. We describe the central tendency of ages with inverse-variance weighted mean (ivwm) and median. We also express the absolute dispersion of ages with the weighted standard deviation, or with the interquartile range (IQR) divided by 1.35, which we here refer to as IQR*.

(U-Th-Sm)/He ages for the three FCT batches are displayed in Figure 5 as sorted box plots. Individual dated-grain data are given in Tables S1–S3, and batch statistics are summarised in Table 1. (U-Th-Sm)/He ages range from 17.95 ± 2.74 Ma (2*s*) to 52.25 ± 7.58 Ma (2*s*). The inverse-variance weighted means of the three batches are close, with values of 27.42 ± 0.24 (*n* = 141), 27.40 ± 0.52 (*n* = 33), and 28.36 ± 0.50 Ma (*n* = 75) (2*s*, standard error of the weighted mean). Sample medians, respectively of 28.03, 28.58 and 29.00 Ma are comparable to the inverse-variance weighted means. Every batch has a positively skewed age distribution (Figure 5).

These estimations of the FCT central age tendency are in good agreement with previous work of Horne *et al*. (2016) where the reported (U-Th-Sm)/He mean age is 28.38 ± 0.73 Ma (2*s*, inverse-variance weighted means multiplied by the square root of the MSWD).

Sample weighted standard deviation values are 4.90, 5.72, and 6.38 Ma respectively, suggesting a high dispersion of ages. IQR* values are 5.31, 7.97, and 9.08 Ma. This latter estimator indicates that even without the bias that outliers may introduce on the calculation of the mean, ages are still significantly dispersed.

Finally, the mean square weighted deviation (MSWD) values are 8.78, 12.72 and 6.60 respectively. With the assumption that measurement uncertainties are accurately calculated, this indicates that another source of dispersion is responsible for the spread of ages.

Comparing our statistics with those of Horne *et al*. (2016), we obtained a similar central tendency on the mean (U-Th-Sm)/He age. Intra-sample dispersion is however clearly different, as our datasets show that both the relative IQR* and the relative weighted standard deviations (RwSD) are significantly higher than those obtained by the previous authors. Furthermore, a significant inter-batch difference in age dispersions is present among our three FCT batches, again revealed by the weighted standard deviations and the IQRs*.

< Table 1 here >
< Figure 5 here >

Cathodoluminescence patterns in FCT zircons

Cathodoluminescence mapping was conducted for zircons of batch FCT-A (see online supporting information Figure S1). Zircons were qualitatively categorised into seven groups, depending on the geometry of the CL zoning, the intensity of CL domains, and the contrast (e.g., Figure 6). Table 2 summarises the characteristics and proportions of each group. Figures 7 and 8 compare the distribution of *in situ* (U-Th-Sm)/He ages for each CL category.

Our CL classification is mostly based on the inner region of the grain because this is where the *in situ* ablation was performed. Therefore, our classification differs from the similar study of Dobson *et al*. (2008) where conventional thermochronometry was performed and where the CL pattern classification reflects the overall grain CL feature.

< Table 2 here >

< Figure 6 here >

< Figure 7 here >

< Figure 8 here >

Normalised eU slopes from LA-ICP-MS pseudo-depth series

We present in Figure 9 the distribution of individual normalised eU slopes (norm. eU slope) among the CL pattern groups, for batch FCT-A. The norm. eU slope is extracted from LA-ICP-MS time-series following the procedure described in Materials and Methods. Cathodoluminescence pattern groups are the same as those presented in Table 2.

Groups 1, 2 and 5 each comprise a significant majority of positive norm. eU slope values, Whisker domains are above the origin axis, and the medians range between +0.0125 and +0.0175 µm^{-1}. These same groups display (U-Th-Sm)/He age distributions mostly below the reference value for zFCT. However, the low number of analyses for these groups prohibits a further discussion of inter-group eU slope dispersion and difference. In contrast, groups 3, 4, 6 and 7 present eU slope distributions with a positive central tendency, medians between 0 and +0.01 µm^{-1} and interquartile ranges falling in a -0.05 to +0.015 µm^{-1} window. For those groups, the interquartile domains are not significantly different, but the whisker domains are.

< Figure 9 here >

We report in Figure 10 the norm. eU slopes compared with (U-Th-Sm)/He ages for all three zFCT batches (A, B, C). Batch FCT-A presents an eU slope Gaussian-shaped distribution centred on +0.005. Interestingly, the highest (U-Th-Sm)/He ages (> 40 Ma) are mostly associated with null slope values. The confidence ellipsoid does not reveal significant correlation between the two variables. Batch FCT-B also presents an eU slope Gaussian-shaped distribution, centred on the zero value. In contrast to FCT-A, the confidence ellipsoid displays a moderate negative correlation. Batch FCT-C presents a negative skewed distribution of norm. eU slopes, with a statistical mode around +0.012 µm^{-1}. Additionally, the confidence ellipsoid reveals a negative correlation between norms. eU slope and (U-Th-Sm)/He ages, similar to batch FCT-B.

< Figure 10 here >

Numerical modelling

The results of the forward numerical modelling are presented in Figures 11 and 12. Modelled *in situ* double-ablation ages are plotted as a function of the normalised eU slope in the left diagrams; the right diagrams present the *in situ* versus conventional ages.

For all the implemented monotonous zoning patterns (except Figure 11a), a linear relationship is found between the double-ablation apparent age and the normalised eU slope. It reveals that the age error can be easily predicted by the relative amplitude of eU depth variation in the U-Th pit when the zoning pattern is known. We also note that a crystal with homogeneous eU mass fraction at the U-Th-Sm sampling site, or in the whole crystal, will have a null normalised eU slope value (e.g., all cases of Figure 11a). Therefore, both *in situ* and conventional trends reasonably intersect the reference age of 28.4 Ma at $x = 0$. Finally, and to simplify the next interpretations, it is easier to consider the apparent age as the measured ^{4}He/eU ratio.

Figure 11 (a–d) shows how the geometry of the U-Th ablation pit affects the age error, for an invariant helium ablation pit (depth and radius equal to 15 µm), and a given monotonous zoning pattern (a step zoning located at a radius of 31.25 µm). In Figure 11a, the model output is straightforward: all normalised eU slope values are null because the U-Th ablation ablates only the inner part of the eU step-zoning, but age errors are either positive or negative (not null) due to alpha-redistribution. Such a feature could be temptingly attributed to some grains of batch FCT-A, where some of the strongest age errors are associated with normalised eU slope values close to zero. In Figure 11b, the model shows a positive correlation between the normalised eU slope and the apparent age: we propose that due to alpha redistribution, the quantity of measured helium comes mainly from the rim zone of the step-zoning, yet this zone is hardly reached by the U-Th-Sm ablation. The quantity of measured ^{4}He therefore increases more than the mean measured eU when the rim is enriched relative to the core (i.e., positive eU slopes). In Figures 11c and d, a negative correlation is found between the normalised eU slope and the apparent *in situ* age, in opposition to the result in Figure 11b. In those cases, when the normalised eU slope increases, the mean measured eU increases more than the mean measured helium and results in a diminution of the apparent age.

Figure 12 (a–d) shows how U-Th monotonous zoning, either linear or in-step, affects the age error, with an invariant double-ablation volumetric geometry (helium with depth = radius = 15 µm, U-Th with depth = radius = 30 µm, which correspond to values used routinely for zFCT age analyses of this study). We observe the correlation previously described, related to the same causes: for the results in Figure 12a, b, and c, the relationship between the normalised eU slope and apparent age is negative, while those in Figure 11d display a positive correlation. Figures 11b and 12d are very alike when one considers the volumetric intersection between the ablation volumes and the eU zoning.

< Figure 11 here >

< Figure 12 here >

Discussion

Bias induced by the double-ablation procedure

Our numerical modelling revealed how the concentric double-ablation micro-sampling strategy leads to an unavoidable age error when U-Th-Sm zoning occurs in the zircon crystal, a concept we will refer to as eU zoning-related double-ablation bias. As for conventional thermochronology (e.g., Hourrigan *et al*. 2005), the resulting age error reflects the difference between the measured ^{4}He/eU isotopic ratio and its true (or at least expected) value. The causes of this bias are however different because the laser-ablation procedure is not subject to alpha crystal-ejection. Instead, the double-ablation age bias results from a complex interplay between the 3D zoning geometry, the extent of alpha-particle redistribution, and volumetric geometries of both ablations.

We propose that two different mechanisms can explain the eU zoning-related double-ablation bias. The first mechanism is due to the redistribution and lateral implantation of ^{4}He particles related to the long alpha stopping distance effect, which we will refer to as the "implantation" effect in the following. The local over- or under-implantation of ^{4}He particles occurs when an eU-rich or eU-poor region of the grain strongly contributes to the measured helium quantity via centrifugal alpha-redistribution, while being erroneously accounted for by the U-Th-Sm sampling and quantification, thus leading to a positive or negative bias, respectively. The geometry of the double-ablation pits used in our procedure (Figure 1) is designed to minimise such effect. However, if an eU-rich or -poor region is strictly contiguous to the external boundary of the U-Th-Sm ablation spot, then ^{4}He particles originating from this aureole can cross the 15 µm distance that separates them from the core of the grain where helium content is determined. This effect is enhanced if the two ablation spots are not perfectly concentric, or if the zircon zoning pattern is not perfectly symmetrical in 3D, thus allowing eU-contrasted aureoles located on the abraded top-half of the grain to be closer to the grain core where ^{4}He is measured.

It is tempting to believe that increasing the size of the second ablation spot will minimise this effect, so that no ^{4}He particles originating from unquantified outer eU aureoles can contribute to the ^{4}He measurement. Indeed, if we consider the average mean stopping distance for the various parent nuclides (17–20 µm), then the final ablation diameter should be increased by more than 10 µm, reaching a total diameter of more than 70 µm, compared with the 60 µm used for the current procedure. However, increasing the diameter from 60 to 70 µm to minimise the zoning bias effect critically depends on zircon size distribution in a sample and can potentially generate another type of bias linked to the preferential picking of larger grains.

Additionally, the simulations reported in Figure 11 provide direct evidence that increasing the size of the U-Th-Sm spot does not reduce the bias. Indeed, when comparing Figure 11b, c and d the real gain in bias minimisation occurs when the contrasted zoning boundary corresponds to the outer rim of the second ablation spot (Figure 11c), whereas when the ablation spot incorporates the zoning boundary (Figure 11d) the bias increases again, even for a larger second spot. This highlights the fact that the natural eU zoning of zircons controls the bias in a complex manner which cannot be addressed simply by spot size adaptation.

The second mechanism is simply related to the fact that the first ablation spot removes completely the core volume of the zircon grain. We refer to this effect as the "blind" effect, in the sense that we cannot determine the U-Th-Sm concentration of this volume, nor that we can determine its ^{4}He contribution. Here again, an age bias will occur if there exists a significant zoning-related eU contrast between the core of the grain and the periphery documented by the second ablation spot. As the inner region (i.e., the first He spot) can be either relatively eU-enriched or eU-depleted compared with the periphery (i.e., the U-Th-Sm spot), it can result in a positive or negative age bias.

In both cases (i.e., "implantation" and "blind" effects), the modelling results (Figure 11) illustrate that a simple core-to-rim eU variation can generate either a positive or a negative error in the calculated (U-Th-Sm)/He age. Thus, when one sample provides crystals with different/opposite eU zoning geometries as can be expected in a detrital sample, the age offset is controlled by the two distinct "implantation" and "blind" effects which cannot be predicted by the norm. eU slope only. The norm. eU slope can however be used to take into account a third effect of potential age bias, which is related to the vicinity of the eU content documented by the second ablation spot to the core of the grain and the related differential redistribution of alpha particles in the zone where ^{4}He is measured. However, this effect is of a second order compared with the two others regarding the final age error.

The importance of the grain size was not directly studied in our numerical modelling, because contrasted grain sizes should not affect whatsoever the double-ablation procedure, as long as the He ablation is targeting a region of the crystal not subject to alpha loss. However, if one uses too contrasted grain sizes during the mounting operation, there is obviously a risk that the bigger grains are less incorporated in the medium than smaller ones, ultimately resulting in over-abrasion for the former, under-abrasion for the latter, with respect to their respective mid-planes. Assuming eU zoning symmetry on both sides of the mid-plane, it appears that differential-abrasion could also be responsible for the eU zoning related bias as described above. A future numerical modelling effort could investigate the importance of such effect.

Dispersion of the zFCT measured data

CL imagery and pseudo-depth profiling documented for our zFCT data are analytical tools that give biased estimates of the eU zoning in the dated crystals. Both methods are biased on different aspects:

(1) In zircons, the existence of CL bands has been linked to the presence of trace elements such as Mn, V, Hf, Yb, Dy, Gd and Tb (see Rubatto and Gebauer 2000, and references therein). Some elements are considered as quenchers of CL emission, because CL intensity is negatively correlated with elemental mass fraction, such as U, Th, or Y (Rubatto and Gebauer 2000, Dobson *et al*. 2008). However, the degree of equivalence between CL intensity and U-Th mass fraction is weak (see figure 4 of Dobson *et al*. 2008 for instance), meaning that a relatively large range of U-Th mass fractions can have a similar CL intensity. Additionally, the CL imagery can only reveal the compositional zoning exposed by the abraded crystal surface (or sub-surface if one considers the interaction volume of the SEM), as opposed to the *in situ* double-ablation 3D geometry, which requires a volumetric quantification of eU zoning.

(2) The depth-profiling can provide biased depth information due to superimposed ablations, as the progressive U-Th-Sm ablation will sample materials in the neighbourhood of the (pre-existing) helium pit, but also from its base, in a minor proportion (see Dickinson *et al*. 2020). Down-hole fractionation, if not corrected, also leads to a biased estimation of the eU variation.

These issues can explain the lack of convincing correlation between CL textural groups and their normalised eU slope distributions for the FCT-A batch. To remove the depth-profile bias, one would need to convert the time-series to a true depth-series (not a pseudo-depth series), but this represents a complex deconvolution, which may be impossible for a concentric double-ablation.

In the end, and due to these various biases, the CL and the normalised eU slope are unsuitable for calculating the age error described in the previous section for a given zoned crystal. While biased, the pseudo-depth profiling still represents a fast and semi-quantitative way to document the volumetric eU variation within a dated crystal, as a direct by-product of the LA-ICP-MS analysis. If the normalised eU slope fails to predict individual (U-Th-Sm)/He errors, its application to a single or several samples can reveal how eU zoning patterns vary among crystals, i.e., the inter-crystal eU zoning variation. This is particularly well illustrated by the FCT batches we analysed: the difference between the three normalised eU slope spectra reveals that inter-sample eU zoning variation is strong, as batch FCT-C displays a wide range of normalised eU slope values while batch FCT-A and B have centred and narrow distributions (Figure 10).

The dispersion of (U-Th-Sm)/He ages due to zoning, simulated and discussed in the previous section, is observed to a similar extent in our zFCT datasets (Figure 7). Potentially, the mean offset of the (U-Th-Sm)/He mean age in a sample may be either negative or positive compared with the true age of the population if one eU zoning pattern is dominant. We propose that the CL textural groups 1, 2 and 6 of batch FCT-A exhibit this effect as their mean (U-Th-Sm)/He ages are either offset negatively (groups 1 and 2) or positively (group 6) (see Figure 9). This effect has also been emphasised by Dobson *et al*. (2008) and Hourrigan *et al*. (2005) in results on FCT using the conventional procedure, either based on CL imagery analysis or eU depth profile.

Zircons from the Fish Canyon Tuff magmatic system are known to be derived from a complex crystallisation history (Bachmann *et al*. 2007). As zFCT zoning patterns are highly variable, Bachmann *et al*. (2007), Vermeesch *et al*. (2012), and Dobson *et al*. (2008) argued that they constitute a risky reference material for calibration on a pairwise basis. On the other hand, the dramatic complexity of zFCT eU-zoning may be considered a worst-case analogue of the diversity of eU-zoning found in the DZ archive of sedimentary rocks, and therefore can constitute a good dataset to estimate the consequences of such zoning-related dispersion on the application of the double-dating procedure to detrital material.

Implications for the dating procedure to be used in a DZ-based source-to-sink study

In order to evaluate how could this eU zoning-related bias affect the dating procedure for a detrital sample, a very simple statistical simulation was conducted that compares the double-ablation and the conventional approaches for the same input parameter (Figure 13). The input consists of a theoretical distribution of true (U-T-Sm)/He ages, as would be recorded in a DZ archive, with three different arbitrary cooling age populations centred on 72 ± 5 Ma, 120 ± 5 Ma and 250 ± 5 Ma (2*s*), in equal proportions (Figure 13a). The systematic ±5 Ma represents the duration of the geological event, unrelated to the measurement uncertainty.

The zFCT dating presented previously was used to build the experimental distribution function of age error for the *in situ* dating procedure, which integrates the eU-zoning related bias discussed before. The zFCT experimental age distribution from FCT-A, -B and -C batches was fitted with a normal distribution, in order to smooth sporadic effects and the weight of outliers to obtain a simpler working double-dating distribution (Figure 13b left-hand diagram). In a similar manner, we also integrated the conventional zFCT data of Horne *et al*. (2016) to create an experimental normal distribution of age error of the conventional dating procedure (Figure 13b right-hand diagram). The resulting functions were then used to create the distributions of (U-Th-Sm)/He age measurements, by applying the age error functions to the starting population (i.e., Figure 13a). In other terms, these outputs represent the distributions of age measurements when the number of grains dated is infinite (Figure 13b).

To finally reproduce the full dating process, the (infinite) distribution of age measurements is sub sampled, in the range n = 50–300 for double-ablation and in the range n = 10–35 for conventional (Figure 13c). This sub sampling is conducted several times (100 runs) in order to qualitatively compare the reproducibility from one sub-sampling to another, and the frequency of representativity (i.e., the likeness between the infinite and the sub sampled distribution of age measurements). Kernel density estimation (KDE) has been used to give a continuous estimate of the probability density function (pdf) (see Vermeesch 2012 for instance). Finally, because the age distribution analysis is generally based on a peak analysis, the positions of the KDE peaks have been highlighted with a red scatter plot for the double ablation procedure and a yellow scatter plot for the conventional procedure (Figure 13c).

The results show that the dating process itself (conventional or double ablation) is obviously responsible for a first and strong alteration of the thermochronometric signal, independent of the number of grains being dated (Figure 13b). In the distribution of age measurements obtained for the double-ablation procedure, the 72 and 120 Ma peaks are superimposed up to their half heights. This is a consequence of the ablation geometry and eU-zoning related bias, but also of the noise injected in the distribution of true ages. Furthermore, a systemic percentage of error generates a more apparent spread for the oldest ages, which leads to a misleading estimation of the peaks' proportions if one compares the heights of pdf peaks instead of their areas. Although appealing, the distribution of conventional age measurements presented here is based on an error function that is idealised; the result of our numerical modelling has proved that the extent of eU-zoning related bias for conventional dating can equal or exceed double-ablation bias (e.g., Figure 12a, c) in some cases. If one considers the double-ablation error function as a worst-case feature (due to strong eU zoning in zFCT), the conventional error function used here is, on the contrary, its best-case counter counterpart (due to a necessary restrictive grain selection for the conventional dating in Horne *et al*. (2016) study).

The number of dated grains is the second parameter that affects the thermochronometric signal (Figure 13c). For the conventional procedure, using a common number of grains per sample (ten to thirty-five grains, as usually reported in the literature), the sub sampled distributions of age measurements allow a correct dating of each peak age (i.e., the horizontal position), but with an incorrect proportion (i.e., the relative height and width) and weak reproducibility from one random draw to the other. For the double-ablation dating procedure, despite the higher number of dated grains per sample, sampling reproducibility is not perfect due to the diffuse shape of the distribution of age measurements itself. The representativity of the sampling become acceptable when 150 to 200 grains are dated, with reduced risk of obtaining spurious peaks. A higher number of dated grains also decreases the vertical dispersion of all peak maxima and permits a better estimation of the actual peaks age's proportion. From a practical point of view, 150 to 200 DZ can be easily dated if the geological sample provides enough zircons. This number is however only indicative, as the number of grains needed in this model is strongly dependent on the starting distribution.

Both dating procedures, in their current implementation (i.e., with uncorrected eU zoning-related bias, or with insufficient dated grains), do not perfectly document the starting distribution in terms of proportions or peak age estimations. They however do not bias the starting distribution in the same manner. The relatively small number of dated grains treated by the conventional procedure prevents a precise appreciation of the height and proportions of the various peaks, whereas its higher precision leads to better documentation of the population age. In contrast, the double-ablation procedure allows the processing of a large number of grains leading to a better definition of the peak proportions, even if the intrinsic larger initial error due to zoning effects alters the precision on the population ages, which is especially visible for older zircon populations. Nevertheless, the double-ablation procedure is able to distinguish with a reasonable accuracy the two youngest populations in this very simulation case, for one hundred dated grains and more.

A detrital thermochronological study aims to reveal signal variability through time using various sedimentary samples of different depositional ages, and generally focuses on the youngest peak age populations. But changes in the thermochronological detrital signal can be caused either by a change of the palaeo-denudation rates, or by a change in the drainage system and source areas (or a mix of both). In such a context, constraining the provenance of the detrital material is fundamental to distinguish one cause from the other. A key advantage of the double-ablation procedure, previously evoked in this study, resides in it simultaneously providing U/Pb dating from the same ablations. For source-to-sink studies, the double dating approach provides a combination of the two ablation-ages in a single grain, providing both denudation and provenance information, giving it a real advantage compared with the conventional procedure.

The morphology of dated grains constitutes one last potential sources of bias for a dating procedure. Pristine, broken, and rounded zircons derived from a sediment sample are to be dated in the same way to avoid selection bias. For conventional dating, to select only pristine crystals reduces the risk of calculating an incorrect alpha ejection correction factor, but it favours the picking of zircons representing the more proximal or less transported sediment sources; besides, to select abraded or broken grains increases the risk of calculating a wrong alpha ejection factor. In contrast, the quality of the double-ablation procedure is less affected by grain morphology and grain size because the *in situ* analysis can avoid crystal regions assumed to be affected by alpha-ejection loss.

< Figure 13 here >

Conclusions

(1) The *in situ* double-ablation procedure, with concentric and successive ablations, can introduce an (U-Th-Sm)/He age bias due to the interplay between (1) eU zoning and alpha-redistribution, and (2) the interfering geometries (radius, depth) of the ablation pits themselves. This so called eU zoning-related double-ablation bias can either lead to age over-scattering if eU zoning exhibits contrasting zoning types, or a systematic offset in the mean age if eU zoning is dominated by one specific zoning pattern.

(2) We introduce the *normalised eU slope*, a proxy that reflects the amplitude of eU variation along a LA-ICP-MS pseudo-depth series. The calculation of this estimator should be based on LA-ICP-MS signals that are corrected for down-hole fractionation. In this study, its ability to predict zFCT individual errors is limited, because it suffers from the use of a pseudo-depth profile rather than an actual depth-profile, owing to a micro-sampling strategy based on concentric and consecutive ablations. Other effects may be involved, such as differential grain abrasion during sample preparation, or due to contrasted eU content between the polished-away and the mounted portion of a grain. Nonetheless, we believe that this estimator can be used in future studies to help to detect age offset or age over-dispersion related to eU zoning if alternative ablation strategies are tested. Finally, if it cannot predict quantitatively the age error, the normalised eU slope is still an interesting estimator of the degree of eU content variation within the dated grains.

(3) The inability to correct the eU zoning-related bias, not only for double-ablation but also for the conventional procedure, implies that a strong error can affect the dating of eU-zoned zircons. We studied how this bias can affect a detrital zircon-based study, with the use of a simple simulation where a synthetic distribution of (U-Th-Sm)/He detrital ages is affected by the analytical limitations of each dating procedure (namely, the estimated age error and the mean sample size). (1) Concerning conventional dating, the procedure brings better analytical precision but with no guarantee and no direct information that eU zoning-related bias is negligible. Even with the strong assumption that such bias is negligible for the studied detrital zircon (i.e., the age error function we chose in our model), representativity between the distributions of true and measured ages is partly reached, due to the insufficient number of grains that is commonly dated (15 to 30) (see also Vermeesch *et al*. 2004). In those conditions, one understands that interpreting the temporal variation of a detrital thermochronological signal across multiple samples is delicate. (2) Concerning the double-ablation procedure, the severe estimated age error we chose translates into a wide dispersion of measured ages that may prevent resolving close peak ages. Yet the number of grains that can be dated with this fast procedure allows a good representativity between the distributions of true and measured ages, and intra- and inter-sample spectra comparison in terms of peak age position and proportions. Finally, the effortless coupling of single-grain U/Pb dating of detrital zircon also provides a robust provenance constraint. It therefore helps to identify and deconvolute the mechanisms that triggered the temporal variation of the detrital thermochronological signal (variation of palaeo-denudation rates or change in the sediment routing system). Ultimately, the double-dating procedure represents an integrated and worthwhile approach for long-term source-to-sink studies.

Acknowledgements

This work is part of the OROGEN research project, funded by TotalEnergies S.A., the BRGM (Bureau de Recherches Géologiques et Minières), and the INSU-CNRS (Institut National des Sciences de l'Univers - Centre National de la Recherche Scientifique). J. Léger was also granted an ANR-10-LABX-21-RESSOURCES21 funding for the prolongation of his doctoral project. The LA-ICP-MS lab of GeoRessources lab is supported by the French National Research Agency through the national program "Investissements d'Avenir" of the Labex Ressources 21 with Reference ANR-10-LABX-21-RESSOURCES21. This work greatly benefited from discussions with Matthias

Bernet (ISTerre, France) and Antoine Crémades (CRPG). Yves Marrocchi is warmly thanked for constant support and sampling of the FCT at South Fork, Colorado. The support of Andreï Lecomte (SCMEM, Université de Lorraine, France) who conducted most of CL acquisitions was highly appreciated. An anonymous reviewer and Dr. Sarah Gilbert (Guest Editor) are warmly thanked for the comments, criticisms, and help they provided in their extensive reviews. We dedicate this work to the memory of Manu Davy, for the support and the kindness he gave for years at the SARM and CRPG facilities. CRPG contribution number 2827. The authors declare no conflict of interest.

Data availability statement

The data that support this study are available in the online supporting information of this article.

References

Bachmann O., Oberli F., Dungan M. A., Meier M., Mundil R. and Fischer H. (2007)
^{40}Ar/^{39}Ar and U-Pb dating of the Fish Canyon magmatic system, San Juan Volcanic field, Colorado: Evidence for an extended crystallization history. **Chemical Geology, 236**, 134–166.

Boyce J.W., Hodges K.V., Olszewski W.J., Jercinovic M.J., Carpenter B.D. and Reiners P.W. (2006)
Laser microprobe (U-Th)/He geochronology. **Geochimica et Cosmochimica Acta, 70**, 3031–3039.

Campbell I.H., Reiners P.W., Allen C.M., Nicolescu S. and Upadhyay R. (2005)
He-Pb double dating of detrital zircons from the Ganges and Indus Rivers: Implication for quantifying sediment recycling and provenance studies. **Earth and Planetary Science Letters, 237**, 402–432.

Dobson K.J., Stuart F.M. and Dempster T.J. (2008)
U and Th zonation in Fish Canyon Tuff zircons: Implications for a zircon (U-Th)/He standard. **Geochimica et Cosmochimica Acta, 72**, 4745–4755.

Filleaudeau P.Y., Mouthereau F. and Pik R. (2011)
Thermo-tectonic evolution of the south-central Pyrenees from rifting to orogeny: Insights from detrital zircon U/Pb and (U-Th)/He thermochronometry. **Basin Research, 24**, 401–417.

Gleadow A., Harrison M., Kohn B., Lugo-Zazueta R. and Phillips D. (2015)
The Fish Canyon Tuff: A new look at an old low-temperature thermochronology standard. **Earth and Planetary Science Letters, 424**, 95–108.

Guenthner W.R., Reiners P.W., Ketcham R.A., Nasdala L. and Giester G. (2013)

Helium diffusion in natural zircon: Radiation damage, anisotropy, and the interpretation of zircon (U-TH)/He thermochronology. **American Journal of Science, 313**, 145–198.

House M.A., Farley K.A. and Stockli D. (2000)
Helium chronometry of apatite and titanite using Nd-YAG laser heating. **Earth and Planetary Science Letters, 183**, 365–368.

Horne A.M., van Soest M. C., Hodges K.V., Tripathy-Lang A. and Hourigan J.K. (2016)
Integrated single crystal laser ablation U/Pb and (U-Th)/He dating of detrital accessory minerals – Proof-of-concept studies of titanites and zircons from the Fish Canyon tuff. **Geochimica et Cosmochimica Acta, 178**, 106–123.

Hourigan J.K., Reiners P.W. and Brandon M.T. (2005)
U-Th zonation-dependent alpha-ejection in (U-Th)/He chronometry. **Geochimica et Cosmochimica Acta, 69**, 3349–3365.

Jochum K.P., Weis U., Stoll B., Kuzmin D., Yang Q., Raczek I., Jacob D.E., Stracke A., Birbaum K., Frick D.A., Günther D. and Enzweiler J. (2011)
Determination of reference values for NIST SRM 610–617 glasses following ISO guidelines. **Geostandards and Geoanalytical Research, 35**, 397–429.

Jourdan S., Bernet M., Hardwick E., Paquette J.-L., Tricart P., Senebier F. and Coeur F. (2018)
Geo-thermochronology of the Saint Antonin basin, south-eastern France. **BSGF - Earth Sciences Bulletin, 189**, 12.

Ketcham R.A. (2005)
Forward and inverse modeling of low-temperature thermochronometry data. **Reviews in Mineralogy and Geochemistry, 58**, 275–314.

Ketcham R.A., Gautheron C. and Tassan-Got L. (2011)
Accounting for long alpha-particle stopping distances in (U-Th-Sm)/He geochronology: Refinement of the baseline case. **Geochimica et Cosmochimica Acta, 75,** 7779–7791.

Lipman P.W., Steven T.A. and Mehnert H.H. (1970)
Volcanic history of the San Juan Mountains, Colorado, as indicated by potassium-argon dating. **Geological Society of America Bulletin, 81**, 2329–2352.

Lipman P., Dungan M. and Bachmann O. (1997)
Comagmatic granophyric granite in the Fish Canyon Tuff, Colorado: Implications for magma-chamber processes during a large ash-flow eruption. **Geology, 25**, 915–918.

Longerich H.P., Jackson S.E. and Günther D. (1996)

Laser ablation inductively coupled plasma-mass spectrometric transient signal data acquisition and analyte concentration calculation. **Journal of Analytical Atomic Spectrometry, 11**, 899–904.

Ludwig K.R. (1998)
On the treatment of concordant uranium-lead ages. **Geochimica et Cosmochimica Acta, 62**, 665–676.

Naeser C.W., Zimmermann R.A. and Cebula G.T. (1981)
Fission-track dating of apatite and zircon: An interlaboratory comparison. **Nuclear Tracks, 5**, 65–72.

Paton C., Woodhead J.D., Hellstrom J.C., Hergt J.M., Greig A. and Maas R. (2010)
Improved laser ablation U-Pb zircon geochronology through robust down-hole fractionation correction. **Geochemistry Geophysics Geosystems, 11.**

Pickering J., Matthews W., Enkelmann E., Guest B., Sykes C. and Koblinger B.M. (2020)
Laser ablation (U-Th-Sm)/He dating of detrital apatite. **Chemical Geology, 548**, 119683.

Rahl J.M., Reiners P.W., Campbell I.H., Nicolescu S. and Allen C.M. (2003)
Combined single-grain (U-Th)/He and U/Pb dating of detrital zircons from the Navajo Sandstone, Utah. **Geology, 31**, 761–764.

Rubatto D. and Gebauer D. (2000)
Use of cathodoluminescence for U-Pb zircon dating by ion microprobe: Some examples from the western Alps. **In: Pagel M., Barbin V., Blanc P. and Ohnenstetter D. (eds), Cathodoluminescence in geosciences. Springer (Berlin, Heidelberg)**, NNN–NNN.

Schmitz M.D. and Bowring S.A. (2001)
U-Pb zircon and titanite systematics of the Fish Canyon Tuff: An assessment of high-precision U-Pb geochronology and its application to young volcanic rocks. **Geochimica et Cosmochimica Acta, 65**, 2571–2587.

Sláma J., Košler J., Condon D.J., Crowley J.L., Gerdes A., Hanchar J.M., Horstwood M.S.A., Morris G.A., Nasdala L., Norberg N., Schaltegger U., Schoene B., Tubrett M.N. and Whitehouse M.J. (2008)
Plešovice zircon – A new natural reference material for U-Pb and Hf isotopic microanalysis. **Chemical Geology, 249**, 1–35.

Tibari B., Vacherat A., Stab M., Pik R., Yeghicheyan D. and Hild P. (2016)
An alternative protocol for single zircon dissolution with application to (U-Th-Sm)/He thermochronometry. **Geostandards and Geoanalytical Research, 40**, 365–375.

Tripathy-Lang A., Hodges K.V., Monteleone B.D. and van Soest M.C. (2013)

Laser (U-Th)/He thermochronology of detrital zircons as a tool for studying surface processes in modern catchments. **Journal of Geophysical Research: Earth Surface, 118**, 1333–1341.

Vacherat A., Mouthereau F., Pik R., Huyghe D., Paquette J.L., Christophoul F., Loget N. and Tibari B. (2017)
Rift-to-collision sediment routing in the Pyrenees: A synthesis from sedimentological, geochronological and kinematic constraints. **Earth-Science Reviews, 172**, 43–74.

Vermeesch P. (2004)
How many grains are needed for a provenance study? **Earth and Planetary Science Letters, 224**, 441–451.

Vermeesch P. (2012)
On the visualisation of detrital age distributions. **Chemical Geology, 312–313**, 190–194.

Vermeesch P., Sherlock S.C., Roberts N.M.W. and Carter A. (2012)
A simple method for *in-situ* U-Th-He dating. **Geochimica et Cosmochimica Acta, 79**, 140–147.

Whitchurch A.L., Carter A., Sinclair H.D., Duller R.A., Whittaker A.C. and Allen P.A. (2011)
Sediment routing system evolution within a diachronously uplifting orogen: Insights from detrital zircon thermochronological analyses from the south-central Pyrenees. **American Journal of Science, 311**, 442–482.

Wiedenbeck M., Allé P., Corfu F., Griffin W.L., Meier M., Oberli F., von Quadt A., Roddick J.C. and Spiegel W. (1995)
Three natural zircon standards for U-Th-Pb, Lu-Hf, trace element and REE analyses. **Geostandards Newsletter, 19**, 1–23.

Wiedenbeck M., Hanchar J.M., Peck W.H., Sylvester P., Valley J., Whitehouse M., Kronz A., Morishita Y., Nasdala L., Fiebig J., Franchi I., Girard J.P., Greenwood R.C., Hinton R., Kita N., Mason P.R.D., Norman M., Ogasawara M., Piccoli P.M., Rhede D., Satoh H., Schulz-Dobrick B., Skår Ø., Spicuzza M.J., Terada K., Tindle A., Togashi S., Vennemann T., Xie Q. and Zheng Y.F. (2004)
Further characterisation of the 91500 zircon crystal. **Geostandards and Geoanalytical Research, 28**, 9–39.

Wolf R.A., Farley K.A. and Silver L.T. (1996)
Helium diffusion and low-temperature thermochronometry of apatite. **Geochimica et Cosmochimica Acta, 60**, 4231–4240.

Appendix A

(U-Th-Sm)/He age calculation and statistics

The inverse-variance weighted-mean (abbreviated as ivwm in the text):

$$\hat{x} = \frac{\sum_i w_i * x_i}{\sum_i w_i} \tag{A1}$$

where $w_i = 1/\sigma_i^2 \; i.e., the\ inverse\ squared\ analytical\ uncertainty\ (1\sigma)$

x_i is $the\ ith\ independant\ observation\ of\ the\ variable\ X$

The standard error of the weighted mean:

$$\sigma(\hat{x}) = \sqrt{\frac{1}{\sum_i 1/\sigma_i^2}} \tag{A2}$$

The weighted sample standard deviation:

$$\sigma_w = \sqrt{\frac{\sum w_i \times (x_i - \hat{x})^2}{\sum w_i}} \tag{A3}$$

The corrected non-weighted sample standard deviation:

$$\sigma_C = \sqrt{\frac{1}{N-1} \sum (x_i - \bar{x})^2} \tag{A4}$$

where $\bar{x}$ is the arithmetic mean.

The mean squared weighted deviation (MSWD):

$$MSWD = \frac{1}{N-1} \sum_i \frac{(x_i - \hat{x})^2}{\sigma_i^2} \tag{A5}$$

We used the relative weighted standard deviation (RwSD) to estimate dispersion around the central value:

$$RwSD\ (\%) = 100 * \frac{\sigma_w}{\hat{x}} \tag{A6}$$

as well as the relative interquartile range (IQR*):

$$IQR^*(\%) = 100 * \frac{IQR}{median} \tag{A7}$$

Appendix B

Methodology for trace element quantification with down-hole fractionation correction

Down-hole fractionation (DF) occurs during laser ablation and leads to inter-element fractionation clearly visible on the time-series (e.g., Figure 2). A correction for DF is therefore needed to separate natural U, Th and Sm variation from DF-induced variation along the ablation time-series.

One way to achieve this is to use homogeneous reference materials where no or minor natural U, Th, Sm variation is expected to occur. This is the case for NIST SRM 610 and 612 glasses, and for some reference zircons (e.g., the 91500 reference zircon, Wiedenbeck *et al*. 1995, 2004). With such materials, the DF-induced U, Th, Sm variation can be isolated and interpolated during the whole ablation session. The DF-correction tends to flatten the U, Th, and Sm time-series for homogeneous material, independently of the absolute value of the concentration.

This approach is similar to the one proposed by Paton *et al*. (2010) in the Iolite software for dealing with geochronometric ratios (e.g., Pb/U ratio). In our correction, the DF-correction is applied after the calculation of concentration, compared with Paton *et al*. (2010), which correct the raw ratio prior to normalisation to a reference material. Applying the DF correction to the concentration signal does not change the mean value of the analyte.

The final workflow we used is the following (adapted from Longerich *et al*. 1996):

(1) Calculate the normalised sensibility value S for the sample (see Longerich *et al*. 1996), corresponding to:

$$S = S_{Analyte,RM} \times S_{Analyte,SAM} \qquad \text{(B1)}$$

where $S_{Analyte,RM} = \frac{R_{AN,RM}}{C_{AN,RM}} \times \frac{\mathrm{C_{IS,RM}}}{\mathrm{R_{IS,RM}}}$ (B2)

and $\mathrm{S_{Analyte,SAM}} = \frac{\mathrm{R_{IS,SAM}}}{\mathrm{C_{IS,SAM}}}$ (B3)

where *R* is the count rate and *C* is the mass fraction; AN: analyte; RM: reference material; SAM: sample.

(2) Calculate the mass fraction of analyte for the sample, corresponding to:

$$\mathrm{C_{Analyte,SAM}} = \mathrm{R_{Analyte,SAM}} \times \mathrm{S} \qquad \text{(B4)}$$

(3) Interpolate the DF-correction based on homogeneous material along the whole ablation session (see Figure 2).

(4) Apply the DF-correction on each analysis, quality control on secondary reference materials (synthetic glass, natural zircon) (see Figure 2).

Supporting information

The following supporting information may be found in the online version of this article:

Table S1. Individual double-ablation (U-Th-Sm)/He dating and eU pseudo-depth profiling on batch FCT-A.

Table S2. Individual double-ablation (U-Th-Sm)/He dating and eU pseudo-depth profiling on batch FCT-B.

Table S3. Individual double-ablation (U-Th-Sm)/He dating and eU pseudo-depth profiling on batch FCT-C.

Figure S1. Cathodoluminescence mapping images for zircons of batch FCT-A.

This material is available from: http://onlinelibrary.wiley.com/doi/10.1111/ggr.00000/abstract
(This link will take you to the article abstract).

Figure captions

Figure 1. Sketch of the *in situ* double-ablation micro-sampling strategy used in our analyses and simulations. A first ablation (orange) is performed with a depth and radius of ~ 15 µm to measure the helium content, then a second ablation (red) is performed with a depth and radius of ~ 30 µm to measure the U-Th-Sm and Pb-REE content. Ablations are performed after the abrasion of the crystal that aimed to expose the core region of the grain, unaffected by alpha-loss. This cartoon represents a simplified vision of the ablation strategy, as the actual superimposed U-Th-Sm ablation also drills in the helium ablation pit floor (e.g., Pickering *et al*. 2020), resulting in a final complex depth profile.

Figure 2. Down-hole fractionation (DF) effect and correction for a typical LA-ICP-MS batch. The left column shows all NIST SRM 610 analyses, with the original eU signal (black line) as calculated following Longerich and al. (1996), the linear model for DF-induced effect (red line), and the DF-corrected eU signal (blue line). The time-dependent DF-correction function was applied to NIST SRM 612 (orange), 91500 (yellow, a U/Pb reference material), and the zFCT (purple). The overall normalised eU slope values derived from the eU signals were compiled as density curves. A small shift of around 0.005 µm^{-1} is observed between the eU slope distributions of NIST SRM 610 and NIST SRM 612, which likely reflects a slight difference in DF-effect between the materials.

Figure 3. (a) Example of a numerical mesh grid where the ^{4}He diffusion and redistribution problem is solved. The *in situ* sampling strategy is represented with colour: the yellow and red nodes indicate the volume where the ^{4}He and eU mass fractions are determined respectively. In detail, the mean mass fractions of ^{4}He and eU are calculated on a finer mesh (not represented here). Please note that the final depth-profile in the numerical model (perfectly cylindrical) differs from the final complex depth-profile of actual analyses (see Pickering *et al*. 2020 for instance). (b) Example of the calculation of the normalised eU slope derived from the modelled eU depth series. The nodal values (blue) are nodes from the resolution mesh grid, for which the linear model (red) is fitted. A moving mean of the nodal eU values is shown (orange) for the sake of visualisation. The normalised eU slope corresponds to the slope of the linear fit divided by its mean value. The same method is adopted for numerical outputs as well as for zFCT analyses.

Figure 4. Example of numerical modelling inputs (see Figure 12b): (a) Core and rim U and Th input mass fractions are gradually set to 100, 200, 300, 400, 500, 750 and 1000 µg g^{-1}. (b) Equivalent calculated pseudo-LA-ICP-MS normalised eU slopes. For (a) and (b), each table cell is equivalent to one point in the numerical modelling results (Figures 11 and 12). Double ablation consists of a first ablation for helium (depth and radius = 15 µm), followed by the second ablation for U and Th (depth and radius = 30 µm). The radius of the modelled spherical crystal is 50 µm. A final cylindrical depth-profile is assumed in the model, which differs from the actual, complex, depth-profile of analyses.

Figure 5. (U-Th-Sm)/He ages obtained for the three FCT batches. Each individual box represents the age with its analytical uncertainty (half box height represents 2*s*). The blue line represents the median of each batch, the pink line (28.4 Ma) is the value reported by Horne *et al*. (2016).

Figure 6. Representative CL images of zircons from the CL groups defined for batch FCT-A (see Table 2 and the text) (scale bar represents 60 µm).

Figure 7. (a) Results of laser ablation (U-Th-Sm)/He dating of zircons of FCT-A. Ages are sorted in increasing order and categorised by colour code depending on their CL zoning pattern group (see Table 2). Individual boxes represent the age with its measurement uncertainty (half-box height represents 2*s*). (b) Density curve (kernel density estimation with a bandwidth of 2 Ma) and histogram of (U-Th-Sm)/He ages.

Figure 8. Box plot of (U-Th-Sm)/He age distribution among the CL zoning pattern groups (see Table 2). The interquartile range is defined as iqr = q3 - q1, and the Whisker domain extends across the data falling inside the [q1–1.5*iqr ; q3+1.5*iqr] window. Values outside this domain are considered here as statistical outliers of the Whisker domain and are represented with a red cross (+). Inverse-variance weighted mean (2*s*) values are given below the diagram.

Figure 9. Box plot of the normalised eU slope distributions among the CL zoning pattern groups for batch FCT-A. The normalised eU slope is derived from the eU pseudo-depth profile of the LA-ICP-MS time-series (see text).

Figure 10. Scatter plot of the norm. eU slope (μg g^{-1} / μm / μg g^{-1}, or μm^{-1}) versus the (U-Th-Sm)/He age for the three FCT batches (A, B, C). Individual measurement uncertainty on the (U-Th-Sm)/He age is given with 2*s* (half-box height). Pink line indicates the reference age of 28.4 Ma (Horne *et al*. 2016). A kernel density estimation (colour heat map) is used to enhance data visualisation, together with a confidence ellipsoid (black dashed line, 68% confidence).

Figure 11. Results from forward numerical modelling with implementation of the double-ablation and conventional procedure (see Figure 4 for an example of numerical inputs). The zoning geometry is invariant (step at radius = 31.25 μm), therefore the conventional ages are the same between the cases in (a), (b), (c) and (d). The double-ablation micro-sampling strategy is variable, as the U-Th ablation radius and depth vary from 20 to 35 μm. The helium ablation radius and depth are invariant with a value of 15 μm. Left hand graphs present the norm. eU slope versus the double-ablation (U-Th-Sm)/He age. Right hand graphs present the double-ablation versus the conventional (U-Th-Sm)/He age. (a) radius and depth of U-Th-Sm pit = 20 μm. (b) radius and depth of U-Th-Sm pit = 25 μm. (c) radius and depth of U-Th-Sm pit = 30 μm. (d) radius and depth of U-Th-Sm pit = 35 μm. The grey boxes indicate the range covered by the conventional ages, corrected for alpha-ejection but not for alpha-redistribution.

Figure 12. Results from forward numerical modelling with implementation of the double-ablation and conventional procedures (see Figure 4 for an example of numerical inputs). The double-ablation micro-sampling strategy is invariant, U-Th (He) ablation radius and depth = 30 μm (15 μm). The zoning geometry is variable, with four different monotonous configurations from core to rim: (a) linear eU zoning. (b) eU step-zoning at radius = 25 μm. (c) eU step-zoning at radius = 31.25 μm. (d) eU step-zoning at radius = 37.5 μm. Left hand graphs axes present the norm. eU slope versus the double-ablation (U-Th-Sm)/He age. Right hand graphs present the double-ablation age versus the conventional (U-Th-Sm)/He age. The grey boxes indicate the range covered by conventional ages, corrected for alpha-ejection but not for alpha-redistribution.

Figure 13. *In situ* double-ablation (left-hand column) and conventional (right-hand column) dating procedures applied to a theoretical age population. (a) Input scenario that represents the theoretical distribution of true ages found in a sediment sample (i.e., the starting distribution in the text). (b) For each column, left-hand diagram presents the empirical and modelled cumulative age error function, and right-hand diagram presents the distribution of age measurement, that is the theoretical distribution of age affected by the overall error. Sources of age error are thoroughly discussed in the text and include eU-zoning related bias and measurement uncertainties. (c) Random sub sampling (*N* = 100 replicates, light grey lines) of the distribution of age measurement (*n* = 50–300 for *in situ* double-ablation dating, *n* = 10–35 for conventional dating). Multiple replicates qualitatively reveal the degree of reproducibility (i.e., how similar are sub sampled age distributions) and representativity (i.e., how similar are the theoretical and the sub sampled age distributions) of each dating procedure. Scatter points represent the maxima of the (light grey) KDE curves.

Table 1.

Summary of results of laser ablation (U-Th-Sm)/He dating on the three batches of FCT. Statistics from Horne *et al*. (2016) are displayed as comparison

Batch		***N***	**Weighted mean (Ma)**	**Standard error of the weighted mean (Ma)**	**Weighted standard deviation (Ma)**	**Corrected non-weighted standard deviation (Ma)**	**Sample RwSD (%)**	**Sample median (Ma)**	**IQR* (Ma)**	**Relative IQR* (Ma)**	**MSWD**
(this study)	FCT-A	141	27.42	0.12	4.9	5.43	17.87	28.03	5.31	18.94	8.78
	FCT-B	33	27.4	0.26	5.72	6.06	20.88	28.58	7.97	27.54	12.72
	FCT-C	75	28.36	0.25	6.38	7.95	22.5	29	9.08	31.31	6.6
Horne *et al* . (2016)		44	28.37	0.17	2.54	2.65	8.95	28.8	2.89	10.03	4.62

Table 2.

Categorisation of Fish Canyon Tuff zircons based on their CL textural aspects (batch FCT-A)

Group number	**Colour code**	**Group name**	**Dominant CL feature, Brief description**	**Number (proportion)**
Group 1	🟪	Bright (high CL intensity) core	The grain has a core domain that is bright i.e., with high CL intensity.	6 (4.5%)
Group 2	🟦	Largely bright	The grain displays high CL intensity almost everywhere, with low contrast.	4 (3.0%)
Group 3	🟩	Grey	The grain exhibits no or little contrast at the 5–10 µm scale. If oscillatory zoning is present but with high spatial frequency, the grain falls in this category. CL-intensity are moderate, not to bright, not to dark.	19 (14.2%)
Group 4	🟨	Multiple CL broad bands	The grain displays multiple broad bands of minimum 5–10 µm width with variable CL intensities and moderate to high contrast.	55 (41.0%)
Group 5	🟧	Largely dark	The grain displays low CL intensity almost everywhere, with low contrast.	6 (4.5%)
Group 6	🟥	Dark (low CL intensity) core	The grain has a core domain that is dark i.e., with low CL intensity.	31 (23.1%)
Group 7		Dark-CL embayment	The grain exhibits one or several utterly dark and lobed domains, that overprint the geometrical textures.	13 (9.7%)

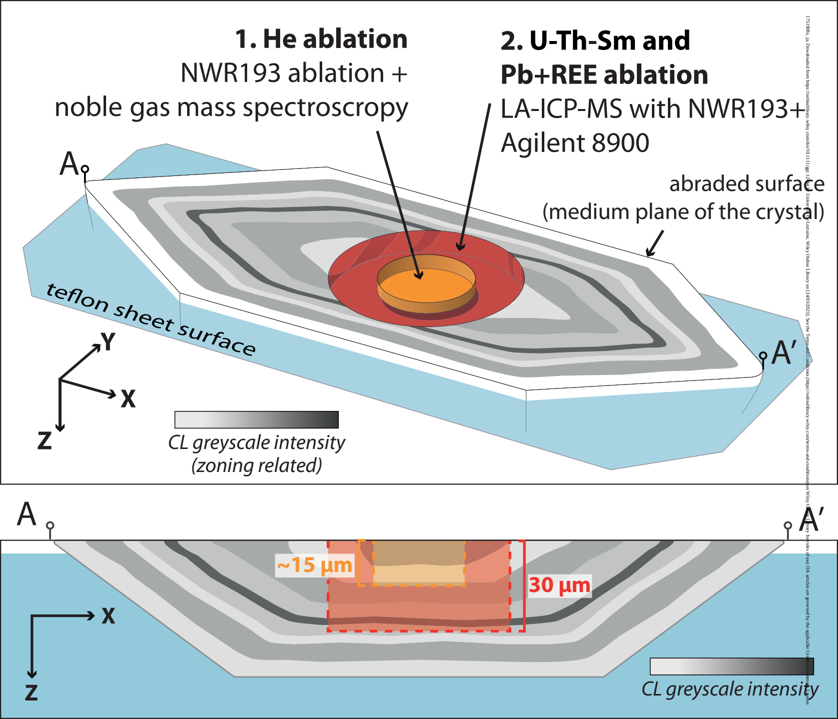
1. He ablation
NWR193 ablation +
noble gas mass spectroscropy
2. U-Th-Sm and
Pb+REE ablation
LA-ICP-MS with NWR193+
Agilent 8900
A
A′
abraded surface
(medium plane of the crystal)
teflon sheet surface
Y
X
Z
CL greyscale intensity
(zoning related)
A
A′
~15 µm
30 µm
X
Z
CL greyscale intensity

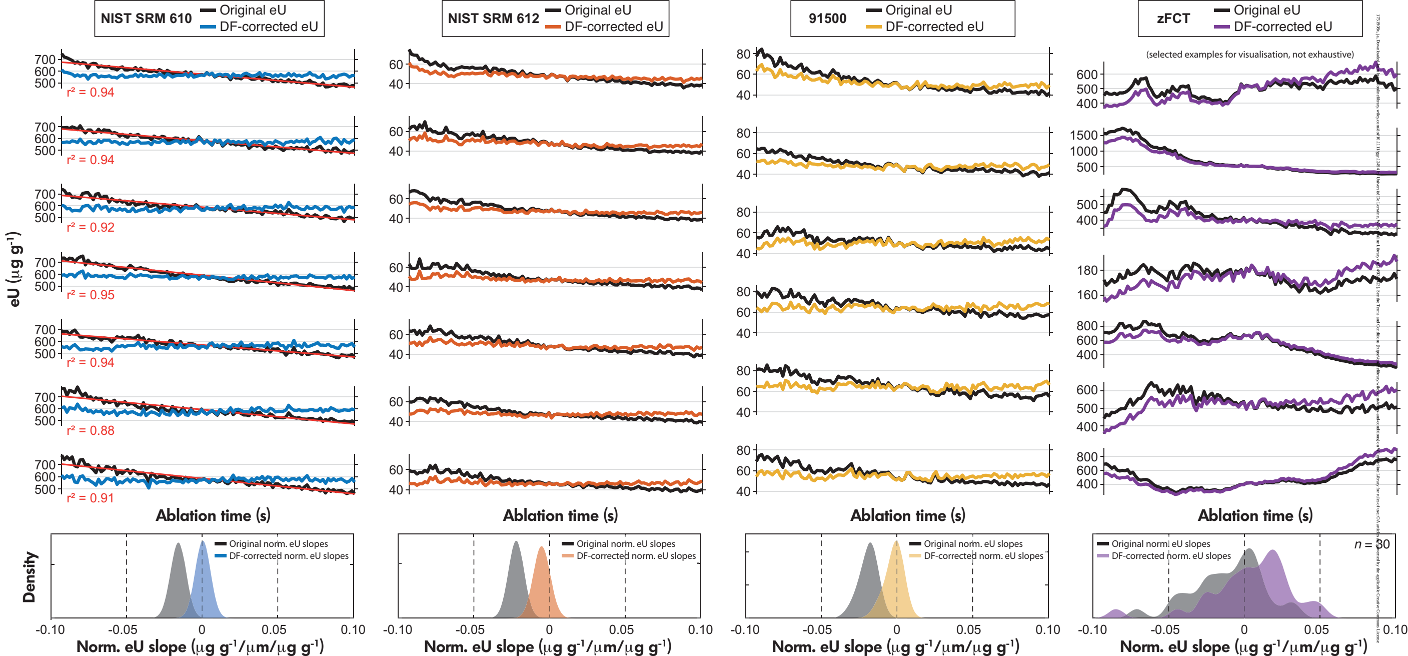
NIST SRM 610
Original eU
DF-corrected eU
NIST SRM 612
91500
zFCT
(selected examples for visualisation, not exhaustive)
eU (μg g⁻¹)
r² = 0.94
r² = 0.94
r² = 0.92
r² = 0.95
r² = 0.94
r² = 0.88
r² = 0.91
700
600
500
60
40
80
1500
1000
400
180
160
800
Ablation time (s)
Density
Original norm. eU slopes
DF-corrected norm. eU slopes
n = 30
-0.10
-0.05
0
0.05
0.10
Norm. eU slope (μg g⁻¹/μm/μg g⁻¹)

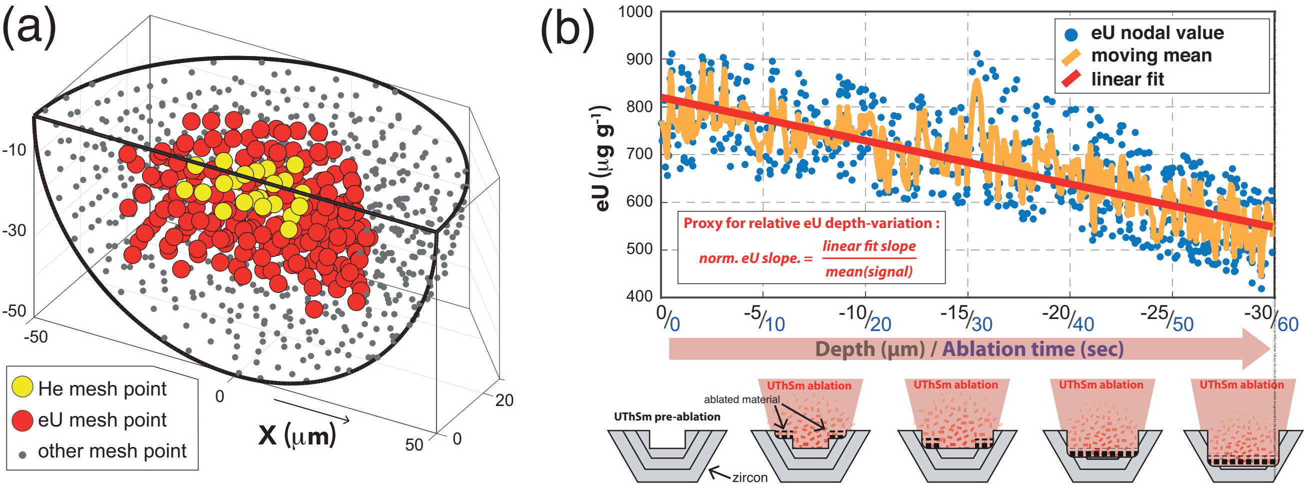
(a)
-10
-30
-50
-50
0
50
20
0
X (μm)
He mesh point
eU mesh point
other mesh point
(b)
1000
900
800
700
600
500
400
eU (μg g^{-1})
eU nodal value
moving mean
linear fit
Proxy for relative eU depth-variation :
norm. eU slope. = linear fit slope / mean(signal)
0/0
-5/10
-10/20
-15/30
-20/40
-25/50
-30/60
Depth (μm) / Ablation time (sec)
UThSm pre-ablation
ablated material
zircon
UThSm ablation
UThSm ablation
UThSm ablation
UThSm ablation

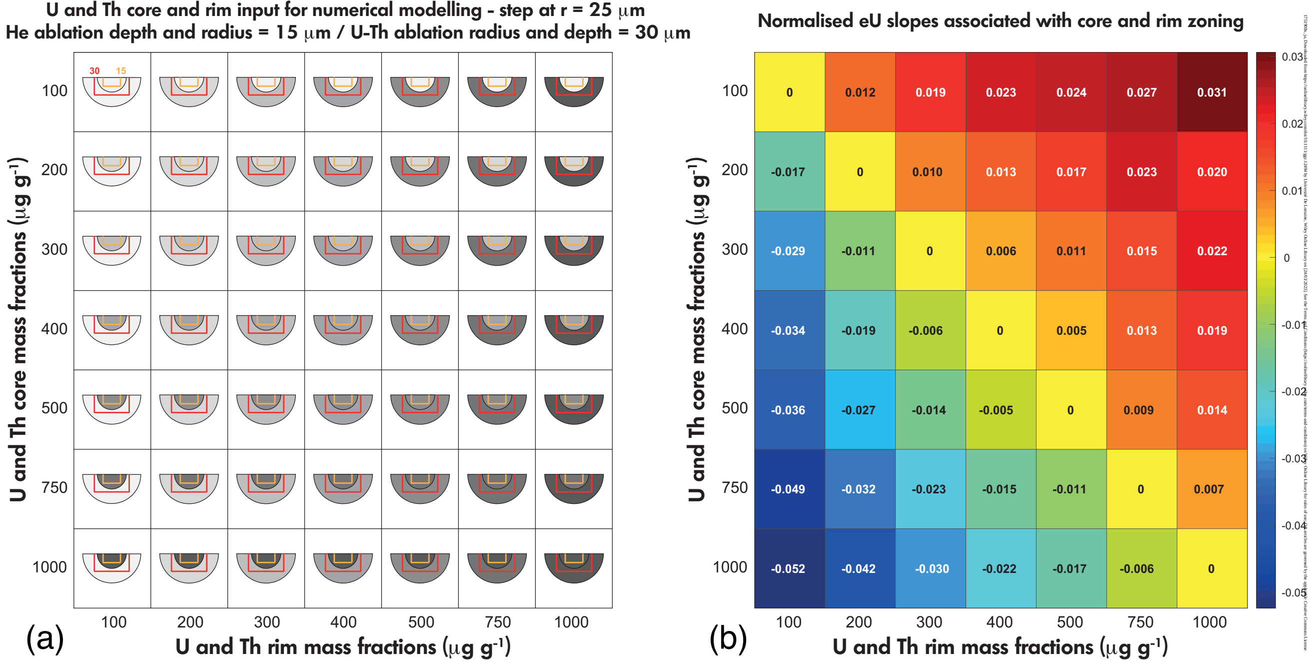

U and Th core and rim input for numerical modelling - step at r = 25 µm
He ablation depth and radius = 15 µm / U-Th ablation radius and depth = 30 µm

Normalised eU slopes associated with core and rim zoning

U and Th core mass fractions (µg g^{-1}) \ U and Th rim mass fractions (µg g^{-1})	100	200	300	400	500	750	1000
100	0	0.012	0.019	0.023	0.024	0.027	0.031
200	-0.017	0	0.010	0.013	0.017	0.023	0.020
300	-0.029	-0.011	0	0.006	0.011	0.015	0.022
400	-0.034	-0.019	-0.006	0	0.005	0.013	0.019
500	-0.036	-0.027	-0.014	-0.005	0	0.009	0.014
750	-0.049	-0.032	-0.023	-0.015	-0.011	0	0.007
1000	-0.052	-0.042	-0.030	-0.022	-0.017	-0.006	0

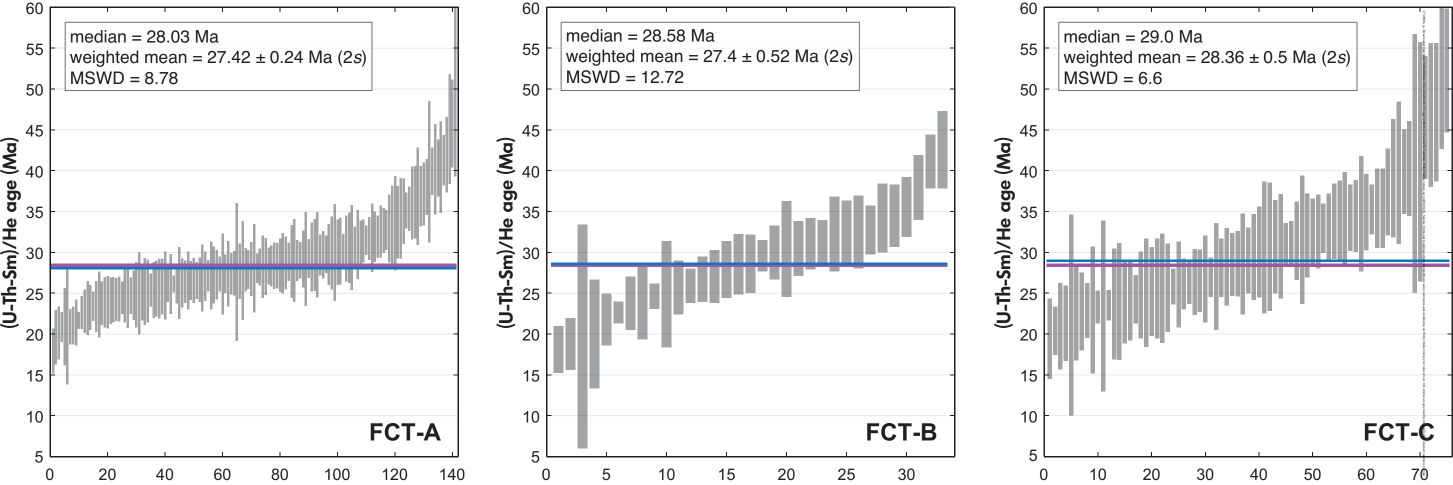
median = 28.03 Ma
weighted mean = 27.42 ± 0.24 Ma (2*s*)
MSWD = 8.78
FCT-A
median = 28.58 Ma
weighted mean = 27.4 ± 0.52 Ma (2*s*)
MSWD = 12.72
FCT-B
median = 29.0 Ma
weighted mean = 28.36 ± 0.5 Ma (2*s*)
MSWD = 6.6
FCT-C
(U-Th-Sm)/He age (Ma)
5
10
15
20
25
30
35
40
45
50
55
60
0
20
40
60
80
100
120
140
0
5
10
15
20
25
30
0
10
20
30
40
50
60
70

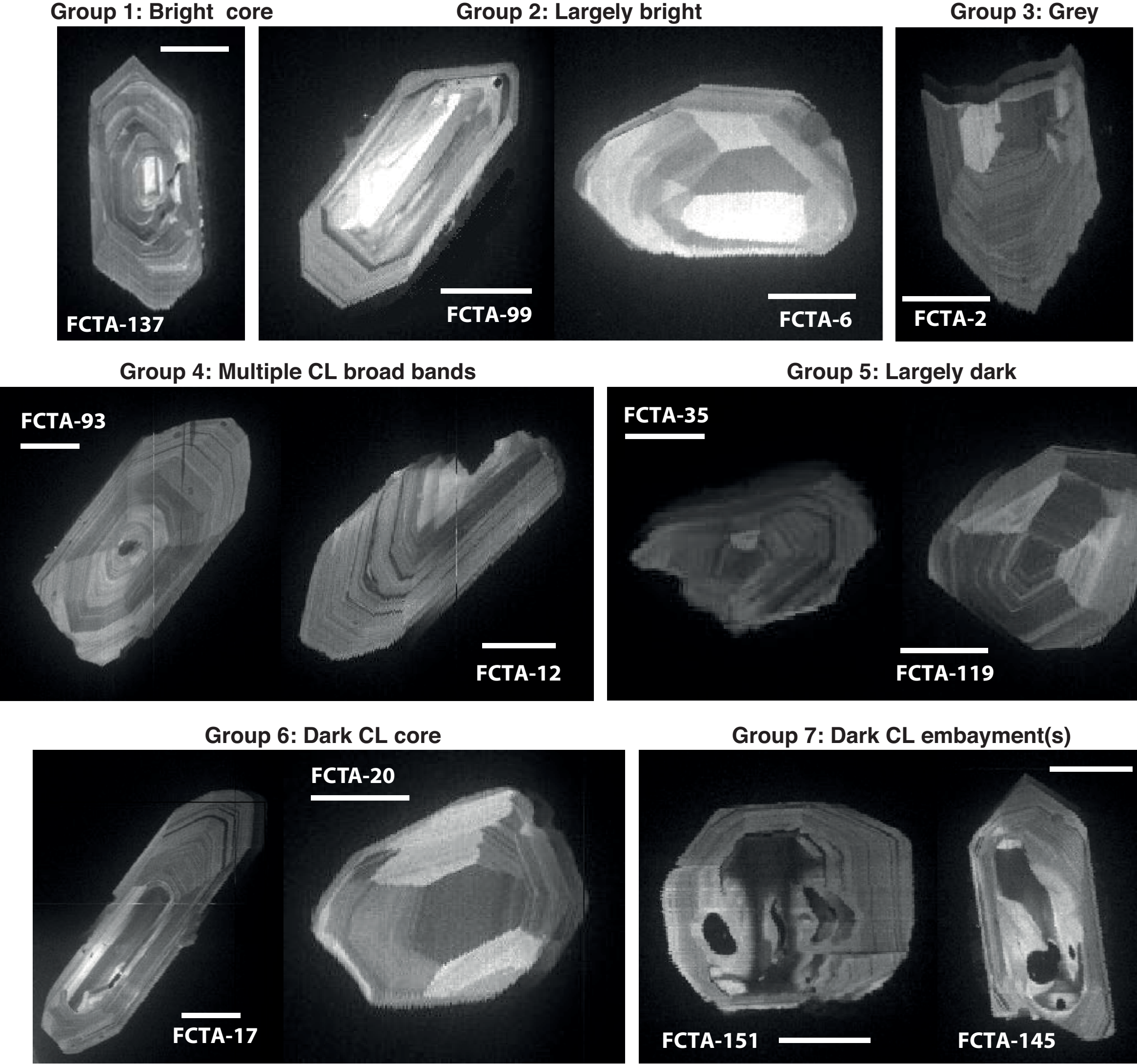
Group 1: Bright core
Group 2: Largely bright
Group 3: Grey
FCTA-137
FCTA-99
FCTA-6
FCTA-2
Group 4: Multiple CL broad bands
Group 5: Largely dark
FCTA-93
FCTA-12
FCTA-35
FCTA-119
Group 6: Dark CL core
Group 7: Dark CL embayment(s)
FCTA-20
FCTA-17
FCTA-151
FCTA-145

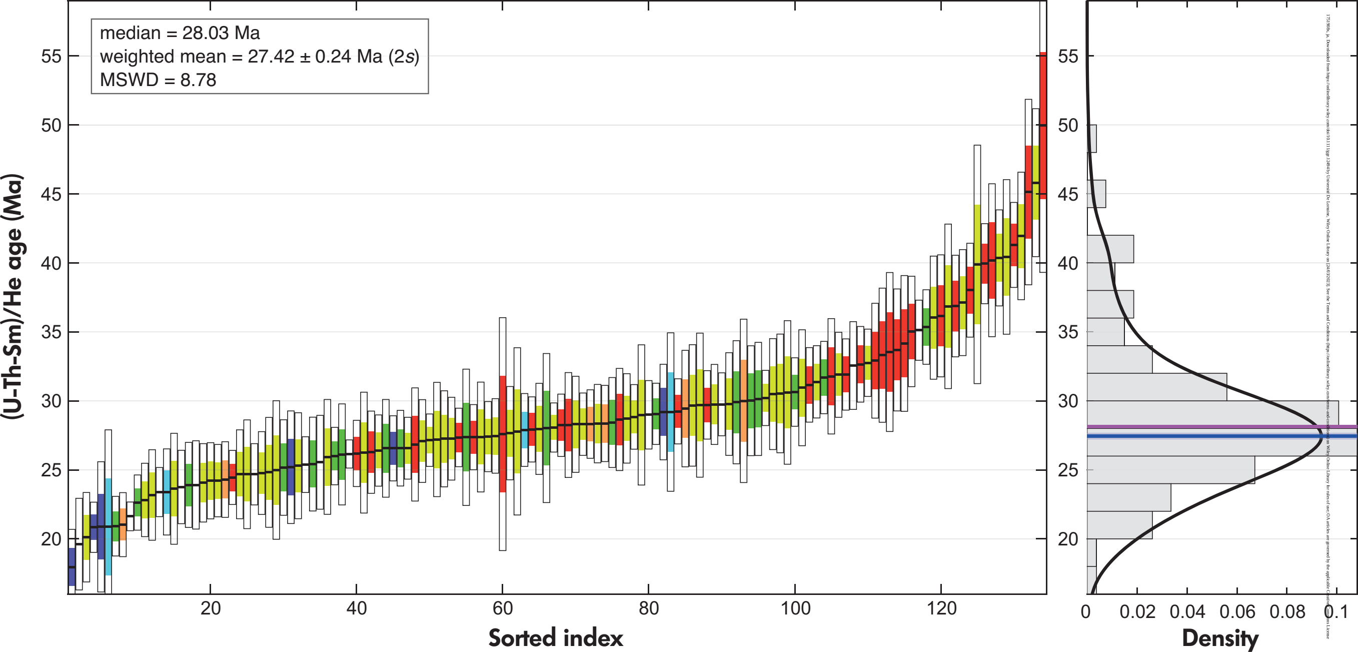
median = 28.03 Ma
weighted mean = 27.42 ± 0.24 Ma (2*s*)
MSWD = 8.78
(U-Th-Sm)/He age (Ma)
55
50
45
40
35
30
25
20
20
40
60
80
100
120
Sorted index
0
0.02
0.04
0.06
0.08
0.1
Density

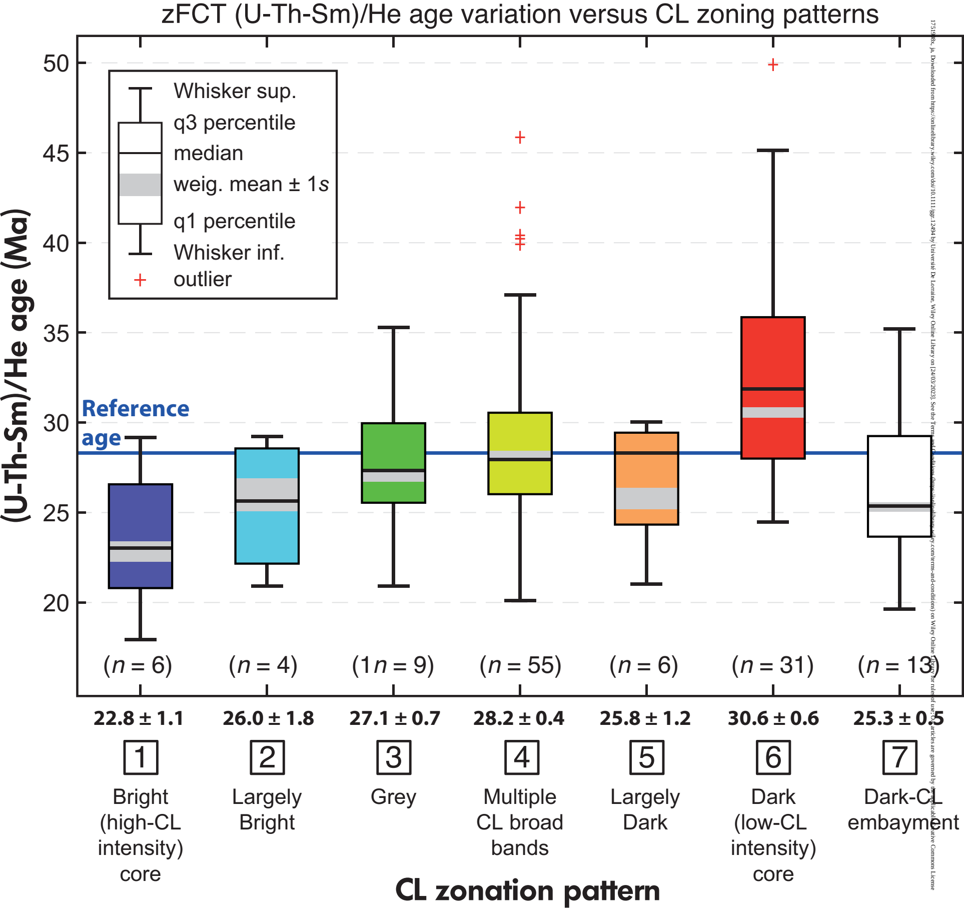
zFCT (U-Th-Sm)/He age variation versus CL zoning patterns
(U-Th-Sm)/He age (Ma)
50
45
40
35
30
25
20
Whisker sup.
q3 percentile
median
weig. mean ± 1s
q1 percentile
Whisker inf.
outlier
Reference age
(n = 6)
(n = 4)
(1n = 9)
(n = 55)
(n = 6)
(n = 31)
(n = 13)
22.8 ± 1.1
26.0 ± 1.8
27.1 ± 0.7
28.2 ± 0.4
25.8 ± 1.2
30.6 ± 0.6
25.3 ± 0.5
1
2
3
4
5
6
7
Bright (high-CL intensity) core
Largely Bright
Grey
Multiple CL broad bands
Largely Dark
Dark (low-CL intensity) core
Dark-CL embayment
CL zonation pattern

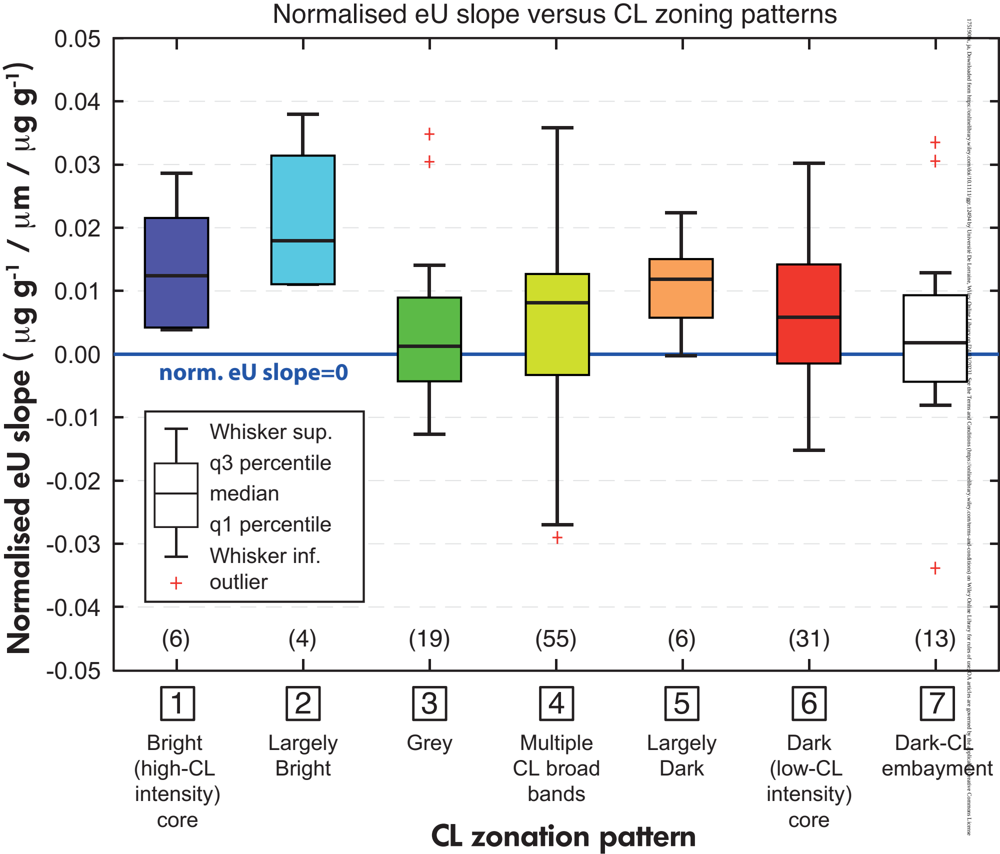
Normalised eU slope versus CL zoning patterns
Normalised eU slope (µg g⁻¹ / µm / µg g⁻¹)
0.05
0.04
0.03
0.02
0.01
0.00
-0.01
-0.02
-0.03
-0.04
-0.05
norm. eU slope=0
Whisker sup.
q3 percentile
median
q1 percentile
Whisker inf.
outlier
(6)
(4)
(19)
(55)
(6)
(31)
(13)
1
Bright (high-CL intensity) core
2
Largely Bright
3
Grey
4
Multiple CL broad bands
5
Largely Dark
6
Dark (low-CL intensity) core
7
Dark-CL embayment
CL zonation pattern

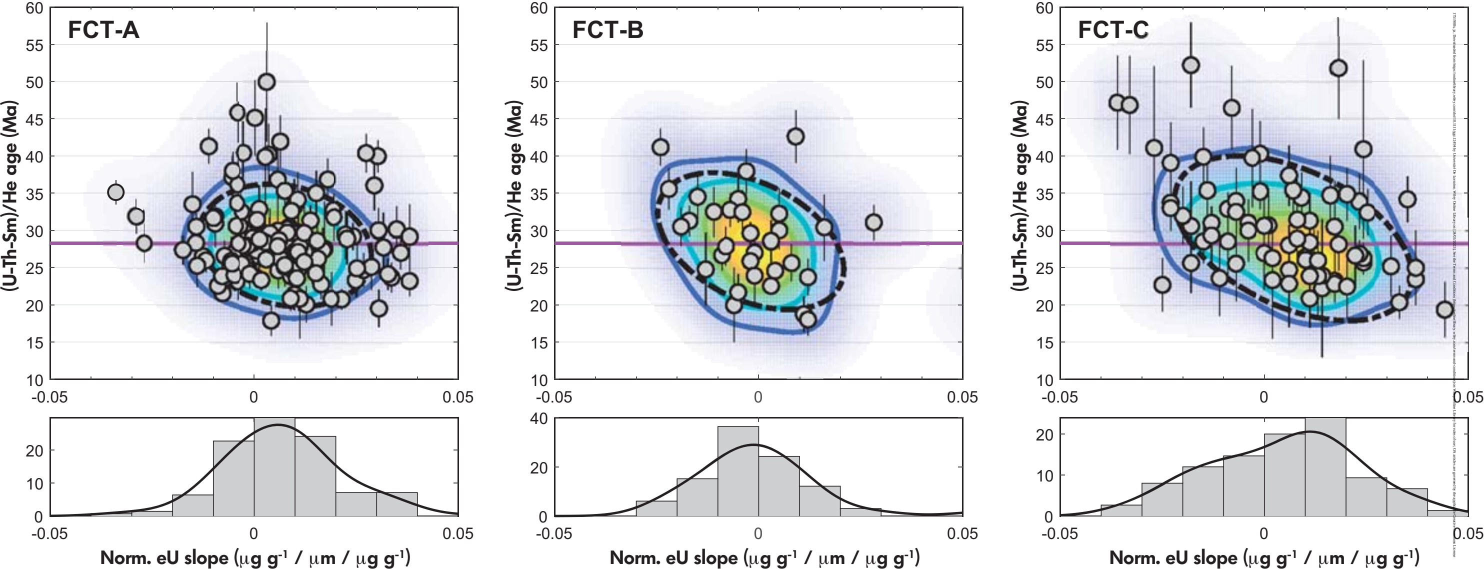
FCT-A
FCT-B
FCT-C
(U-Th-Sm)/He age (Ma)
60
55
50
45
40
35
30
25
20
15
10
-0.05
0
0.05
40
20
10
0
Norm. eU slope (μg g⁻¹ / μm / μg g⁻¹)

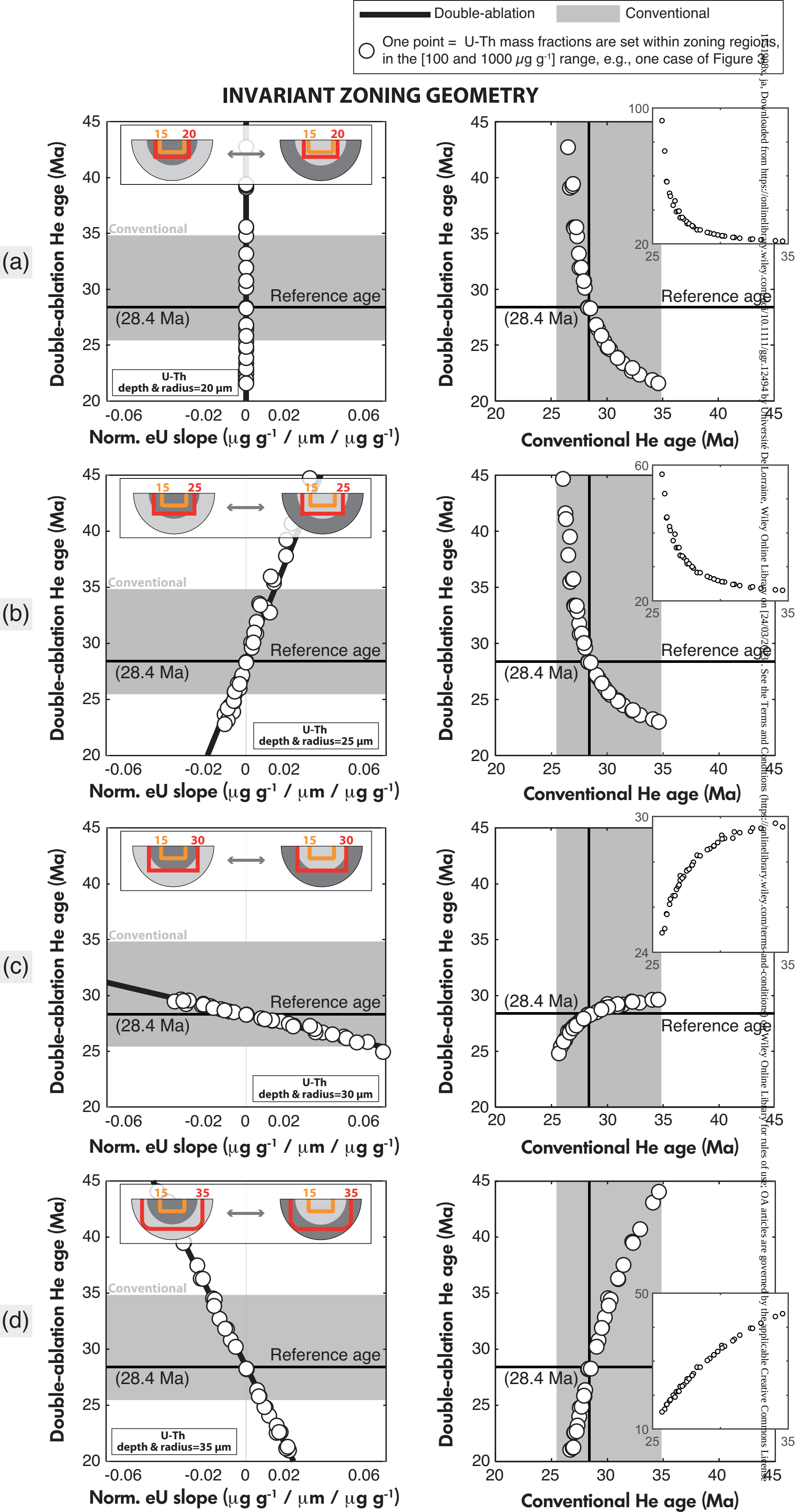
Double-ablation
Conventional
One point = U-Th mass fractions are set within zoning regions, in the [100 and 1000 µg g⁻¹] range, e.g., one case of Figure 3
INVARIANT ZONING GEOMETRY
(a)
(b)
(c)
(d)
15
20
25
30
35
Conventional
Reference age
(28.4 Ma)
U-Th depth & radius=20 µm
U-Th depth & radius=25 µm
U-Th depth & radius=30 µm
U-Th depth & radius=35 µm
Double-ablation He age (Ma)
Norm. eU slope (µg g⁻¹ / µm / µg g⁻¹)
Conventional He age (Ma)
-0.06
-0.02
0
0.02
0.06
20
25
30
35
40
45
100
60
24
50
10

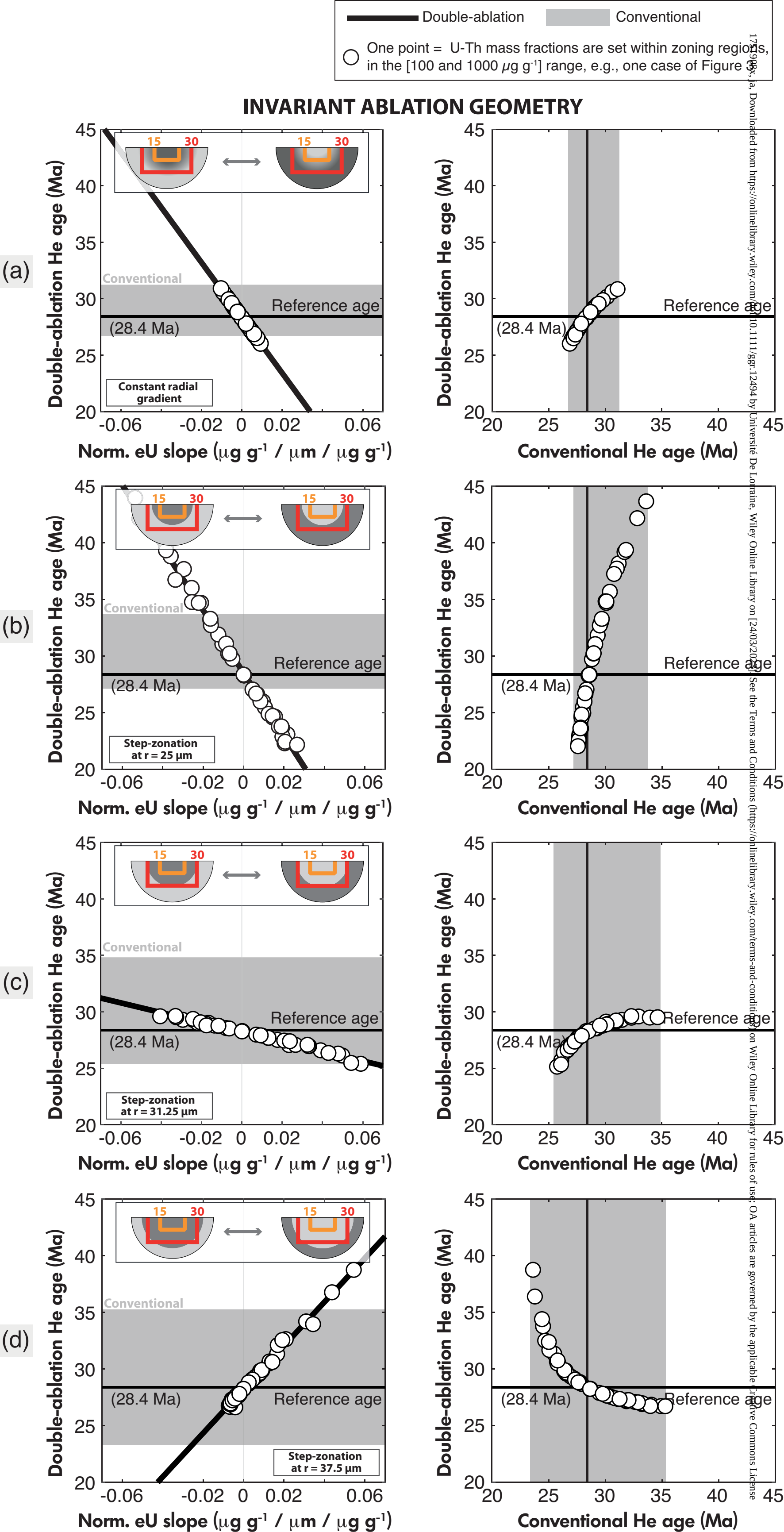
Double-ablation
Conventional
One point = U-Th mass fractions are set within zoning regions, in the [100 and 1000 μg g-1] range, e.g., one case of Figure 3
INVARIANT ABLATION GEOMETRY
(a)
(b)
(c)
(d)
15
30
Conventional
Reference age
(28.4 Ma)
Constant radial gradient
Step-zonation at r = 25 μm
Step-zonation at r = 31.25 μm
Step-zonation at r = 37.5 μm
Double-ablation He age (Ma)
Norm. eU slope (μg g-1 / μm / μg g-1)
Conventional He age (Ma)
-0.06
-0.02
0
0.02
0.06
20
25
30
35
40
45

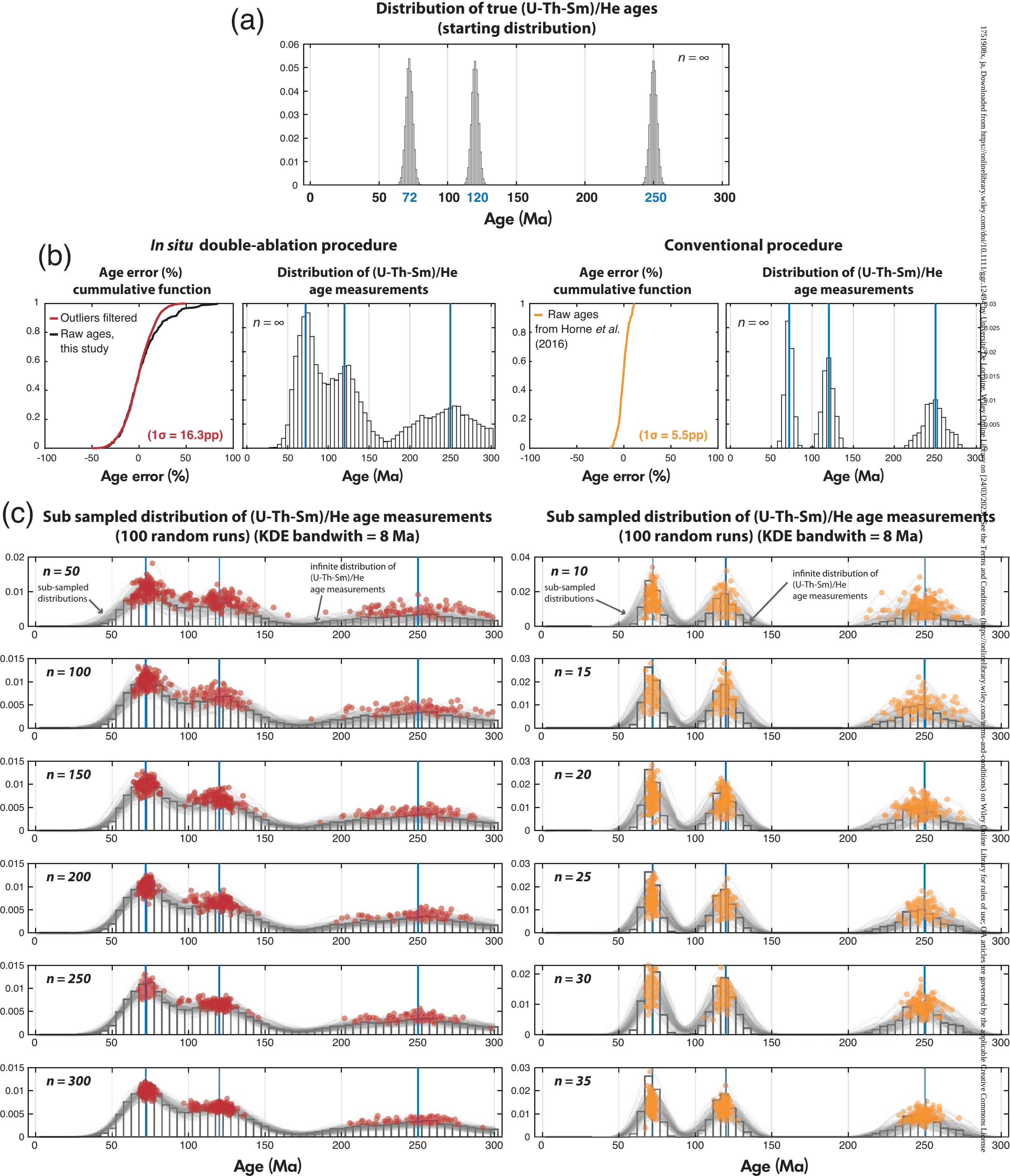
(a)
Distribution of true (U-Th-Sm)/He ages (starting distribution)
n = ∞
72
120
250
Age (Ma)
(b)
In situ double-ablation procedure
Age error (%) cummulative function
Outliers filtered
Raw ages, this study
(1σ = 16.3pp)
Age error (%)
Distribution of (U-Th-Sm)/He age measurements
n = ∞
Age (Ma)
Conventional procedure
Age error (%) cummulative function
Raw ages from Horne et al. (2016)
(1σ = 5.5pp)
Age error (%)
Distribution of (U-Th-Sm)/He age measurements
n = ∞
Age (Ma)
(c)
Sub sampled distribution of (U-Th-Sm)/He age measurements (100 random runs) (KDE bandwith = 8 Ma)
n = 50
sub-sampled distributions
infinite distribution of (U-Th-Sm)/He age measurements
n = 100
n = 150
n = 200
n = 250
n = 300
Age (Ma)
Sub sampled distribution of (U-Th-Sm)/He age measurements (100 random runs) (KDE bandwith = 8 Ma)
n = 10
sub-sampled distributions
infinite distribution of (U-Th-Sm)/He age measurements
n = 15
n = 20
n = 25
n = 30
n = 35
Age (Ma)